PIK Report

No. 84

WELL BALANCED FINITE VOLUME METHODS FOR NEARLY HYDROSTATIC FLOWS

Nicola Botta, Rupert Klein,
Susanne Langenberg, Susanne Lützenkirchen

POTSDAM INSTITUTE
FOR
CLIMATE IMPACT RESEARCH (PIK)

Corresponding author:
Dr. Nicola Botta
Potsdam Institute for Climate Impact Research
P.O. Box 60 12 03, D-14412 Potsdam, Germany
Phone: +49-331-288-2657
Fax: +49-331-288-2695
E-mail: Nicola.Botta@pik-potsdam.de

Herausgeber:
Dr. F.-W. Gerstengarbe

Technische Ausführung:
U. Werner

POTSDAM-INSTITUT
FÜR KLIMAFOLGENFORSCHUNG
Telegrafenberg
Postfach 60 12 03, 14412 Potsdam
GERMANY
Tel.: +49 (331) 288-2500
Fax: +49 (331) 288-2600
E-mail-Adresse:pik@pik-potsdam.de

ISSN 1436-0179 POTSDAM, AUGUST 2003

Abstract:

Recent trends towards the construction of mass and energy conserving, non-hydrostatic, and fully compressible flow models for purposes of numerical weather prediction and regional climate modelling motivate the present work. In this context, a proper numerical representation of the dominant hydrostatic balance is of crucial importance: unbalanced truncation errors can induce unacceptable spurious motions, in particular near steep topography.

In this paper we develop a new strategy for the construction of discretizations that are "well-balanced" with respect to dominant hydrostatics. The popular subtraction of a "hydrostatic background state" is avoided by the introduction of local, time dependent hydrostatic reconstructions. Balanced discretizations of the pressure gradient and the gravitation source term are achieved through a judicious implementation of a "discrete Archimedes' buoyancy principle".

This strategy is applied to extend an explicit standard finite volume Godunov-type scheme for compressible flows with minimal modifications. We plan to address a large time step semi-implicit version of the scheme in future work. The resulting method inherits its conservation properties from the underlying base scheme and has three distinct and desirable features: (i) It is exactly balanced, even on curvilinear grids, for a large class of near-hydrostatic flows. (ii) It directly solves the full compressible flow equations while avoiding the non-local, possibly time-consuming computation of a (slowly time-dependent) background state. (iii) It is robust against details of the implementation, such as the choice of slope limiting functions, or the particulars of boundary condition discretizations.

CONTENTS

1. INTRODUCTION

Atmospheric motions on scales relevant for numerical weather prediction and climate modeling are small perturbations of some hydrostatic state, see [14], [35], [4], [23]. Albeit small, such perturbations are relevant and models based on the Euler equations of compressible fluid mechanics, which do not explicitly assume a hydrostatic balance, have been introduced for research and operational purposes, [9]. For the present purposes it suffices to consider the equations for a dry atmosphere without rotation. These equations are

$$\begin{aligned} \rho_t + \nabla\cdot(\rho\boldsymbol{v}) &= 0 \\ (\rho\boldsymbol{v})_t + \nabla\cdot(\rho\boldsymbol{v}\circ\boldsymbol{v}) + \nabla p &= -\rho\nabla\Phi \\ (\rho e + \rho\Phi)_t + \nabla\cdot((\rho e + p + \rho\Phi)\boldsymbol{v}) &= 0 \end{aligned} \tag{1}$$

together with a state equation for the pressure $p := \varphi(\rho, \rho\boldsymbol{v}, \rho e)$, a time independent gravity potential Φ and suitable initial and boundary conditions. Nearly hydrostatic motions are such that

$$(\nabla p + \rho\nabla\Phi)\cdot\boldsymbol{k} \;=\; O(\epsilon) \;\ll\; |\nabla p\cdot\boldsymbol{k}| \;=\; O\left(|\rho\nabla\Phi\cdot\boldsymbol{k}|\right) \tag{2}$$

where $\boldsymbol{k} := \nabla\Phi/|\nabla\Phi|$ is a unit vector aligned with the acceleration of gravity and ϵ is of the order of magnitude of $(\rho\boldsymbol{v})_t\cdot\boldsymbol{k}$. Importantly, the smallness of ϵ is due to cancellation of almost equal quantities and the "vertical" pressure gradient $\nabla p\cdot\boldsymbol{k}$ does not vanish as $\epsilon \to 0$. For nearly hydrostatic motions, standard numerical approximations for (1) are either inaccurate or unacceptably expensive. A detailed analysis will be presented in section 2, but the reason for inaccuracy is obvious: On grids of grid spacing h, r-th order approximations to ∇p, $\rho\nabla\Phi$ introduce local truncation errors (LTE) of order h^r. Depending on the grid spacing h and on the actual value of ϵ, these spurious accelerations can be orders of magnitude larger than the true vertical acceleration $(\rho\boldsymbol{v})_t\cdot\boldsymbol{k}$.

To motivate this quantitatively, consider a typical low Mach number flow, i.e., $M \ll 1$, with a horizontal scale of $10\,\mathrm{km}$. Its computational representation would necessitate a non-hydrostatic model. Let its vertical characteristic scale be d, and the pressure scale height $D \approx 10\,\mathrm{km}$. In the absence of strong acoustic modes, deviations of pressure from a nearly time invariant background pressure distribution are then of order $O(M^2)$, as is known from low Mach number asymptotic theories [39], [22]. Vertical

accelerations scale as $|dw/dt| \approx M^2 p_{\rm ref}/(\rho_{\rm ref}\, d)$, and we find that

$$\frac{\left|\dfrac{dw}{dt}\right|}{\left|\dfrac{1}{\rho}\dfrac{\partial p}{\partial z}\right|} = O\left(M^2\frac{D}{d}\right) := O(\epsilon)$$

For bulk motions that affect the entire pressure scale height we have $d \approx D$ and $\epsilon = O(M^2)$.

If we require next that the relative (dimensionless) LTEs of a second order accurate numerical computation, i.e. LTEs $\approx (h/D)^2$, are at least by one order of magnitude smaller than ϵ, then we obtain the following requirement on the vertical grid spacing h:

$$\left(\frac{h}{D}\right)^2 < 0.1\epsilon \approx 0.1\, M^2\frac{D}{d}$$

For realistic flow Mach numbers $M \approx 0.03$ and situations in which $d \approx D$, this estimate yields

$$\frac{h}{D} < 0.01\,.$$

This corresponds to vertical resolutions of 100 layers, which is at the limits of feasibility of production runs in NWP or regional climate modelling.

The problem sketched above is typical. It always occurs in the approximation of nearly balanced solutions, the balance being often between *flux divergence* and *source term*. It also arises in the numerical solution of the shallow water equations with bottom topography, in steady state reactive flows, and in many other fields. Numerical methods conceived to cope with this problem are called *well balanced methods*, see [6], [16], [19], [31]. A natural approach for constructing well balanced methods is via balanced solutions. For nearly hydrostatic flows these are functions $p^{(0)}$, $\rho^{(0)}$ such that

$$(\nabla p^{(0)} + \rho^{(0)}\nabla\Phi)\cdot\boldsymbol{k} = 0 \tag{3}$$

If both $\nabla p\cdot\boldsymbol{k}$ and $\rho\nabla\Phi\cdot\boldsymbol{k}$ are order ϵ deviations from $\nabla p^{(0)}\cdot\boldsymbol{k}$, $\rho^{(0)}\nabla\Phi\cdot\boldsymbol{k}$ respectively, i.e.

$$\nabla\,(p - p^{(0)})\cdot\boldsymbol{k} = O(\epsilon) \qquad (\rho - \rho^{(0)})\nabla\Phi\cdot\boldsymbol{k} = O(\epsilon)\,, \tag{4}$$

then $p^{(0)}$, $\rho^{(0)}$ can be used to rewrite (1.2) as

$$(\rho\boldsymbol{v})_t \;+\; \nabla\cdot(\rho\boldsymbol{v}\circ\boldsymbol{v}) + \nabla\delta p \;=\; -\delta\rho\nabla\Phi$$

with $\delta p := p - p^{(0)}$, $\delta\rho := \rho - \rho^{(0)}$ and both $\nabla\delta p\cdot\boldsymbol{k}$ and $\delta\rho\nabla\Phi\cdot\boldsymbol{k}$ of order ϵ. Any r-th order approximate gradient operator will then lead to well balanced LTEs of order ϵh^r.

The problem is, of course, that of computing $p^{(0)}$, $\rho^{(0)}$. In many models for numerical weather forecasting (NWF) and climate research $p^{(0)}$, $\rho^{(0)}$ are approximated by time independent horizontally constant "reference" hydrostatic profiles. In general, these functions satisfy (3) but not (4) leading to LTE which do not scale with ϵ. One can argue that, for short time NWF, good approximations for $p^{(0)}$, $\rho^{(0)}$ can be extracted from the initial data. In climate simulations, however, these approximations may significantly differ, after some finite time, from the slowly evolving hydrostatic components $p^{(0)}$, $\rho^{(0)}$.

Numerical methods for reducing the LTE associated with the discretization of ∇p have been proposed over the past three decades, see [7], [34], [43] and, more recently, [41], [24] and references therein. In all these approaches the governing equations – hydrostatic or non-hydrostatic Boussinesq approximations and, more recently, full compressible Navier-Stokes equations – are not formulated in a Cartesian coordinate system, say (x, z) for horizontal and vertical coordinate, respectively. Instead, a coordinate transformation to curvilinear terrain following coordinates (ξ, ς) is introduced, e.g., as proposed in [13]. In this framework, approximations to differential operators like $\partial p/\partial x$ are computed by summing up products between finite difference approximations to $\partial p/\partial \xi$, $\partial p/\partial \varsigma$ (taken along the grid coordinate lines) and approximations of the metric terms $\partial \xi/\partial x$, $\partial \varsigma/\partial x$. In this context, the balancing problem consists, roughly speaking, of finding approximations to these terms that minimize the LTE associated with $\partial p/\partial x$.

Here we follow a novel approach. It relies on a conservative finite volume formulation of the governing equations with vectors described in a Cartesian frame of reference. This is canonical in finite volume methods, but does not mean that one uses also a Cartesian computational grid, see figure 1. Moreover, the approach employs local approximations of $p^{(0)}$, $\rho^{(0)}$ and a discrete version of Archimedes' buoyancy principle.

Consider standard finite volume approximations of the exact pressure gradient ∇p and of the exact source term $\rho \nabla \Phi$. Let P_i, R_i be approximations of p, ρ on a cell c_i of boundary ∂c_i. Then, finite volume approximations of the cell averages $\delta_{c_i}(\nabla p)$, $\delta_{c_i}(\rho \nabla \Phi)$ of ∇p, $\rho \nabla \Phi$ on c_i read

$$\begin{aligned} \delta_{c_i}(\nabla p) &\approx \frac{1}{|c_i|} \oint\limits_{\partial c_i} P_i \, \boldsymbol{n} \, dS \\ \delta_{c_i}(\rho \nabla \Phi) &\approx \frac{1}{|c_i|} \int\limits_{c_i} R_i \nabla \Phi \, dV \end{aligned} \tag{5}$$

where $\boldsymbol{n}$ is the unit vector normal to ∂c_i and pointing outwards, see figure 1, and we have used the divergence theorem to replace integration on c_i by a boundary integral in (5.1).

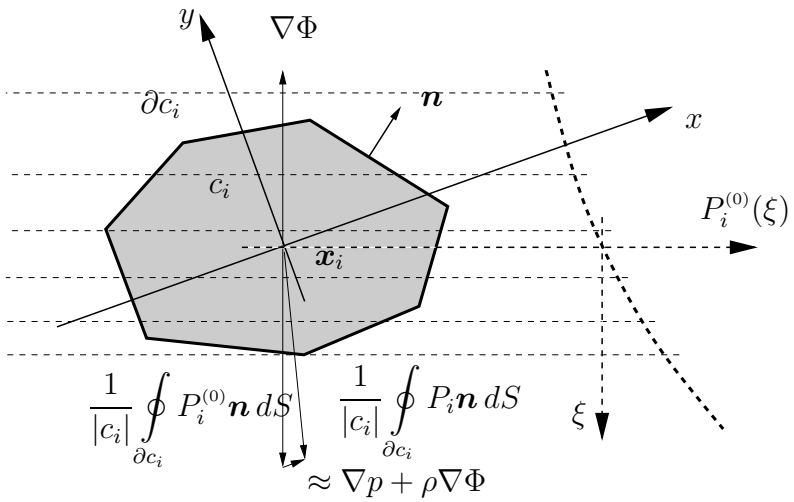

FIG. 1. Control volume c_i, acceleration of gravity $-\nabla\Phi$, local hydrostatic pressure $P_i^{(0)}$ and approximate $\nabla p + \rho\nabla\Phi$.

Notice that, in numerical methods, the integrals on the right hand side are usually approximated by finite sums. This fact, however, is not relevant for our discussion. Let $P_i^{(0)}$, $R_i^{(0)}$ be exact solutions of

$$\nabla P_i^{(0)} + R_i^{(0)}\nabla\Phi = 0$$

with $P_i^{(0)}$, $R_i^{(0)}$ interpolating P_i, R_i in the center x_i of c_i. Using these functions, the integral on the right hand side of (5.2) can be replaced, with second order accuracy, by

$$\begin{aligned}\frac{1}{|c_i|}\int_{c_i} R_i\nabla\Phi\,dV &= \frac{1}{|c_i|}\int_{c_i} R_i^{(0)}\nabla\Phi\,dV + O(h_i^2)\\ &= -\frac{1}{|c_i|}\oint_{\partial c_i} P_i^{(0)}\,\boldsymbol{n}\,dS + O(h_i^2)\end{aligned} \tag{6}$$

We have thus approximated the source term in discrete gradient form by replacing the volume integral of $R_i^{(0)}\nabla\Phi$ by means of the boundary integral of $P_i^{(0)}\,\boldsymbol{n}$. This is what we referred to as discrete Archimedes' principle. The above formulation yields the following second order finite volume approximation to the average of $\nabla p + \rho\nabla\Phi$ over c_i:

$$\delta_{c_i}(\nabla p + \rho\nabla\Phi) \approx \frac{1}{|c_i|}\oint_{\partial c_i}\left(P_i - P_i^{(0)}\right)\,\boldsymbol{n}\,dS \tag{7}$$

This formulation and a careful construction of $P_i^{(0)}$ allows us to control the scaling of the LTE associated with the discretization of $\nabla p + \rho\nabla\Phi$. A few remarks are in order here:

The approach outlined above is independent of the number of space dimensions and does not require any special grid arrangement. In particular, it does not require any grid coordinate to be aligned with the direction of the acceleration of gravity $\nabla\Phi$ and can be used both on structured and on unstructured, e.g., triangular grids, see x, y coordinate system in figure 1.

In the proposed formulation, numerical approximations to the gravity source term are always computed as vector quantities. As shown in (7), this is done by using exactly the same discrete gradient operator which is used for the computation of the approximate pressure gradient. This is crucial for guaranteeing the proper scaling of the LTEs associated with the discretization of $\nabla p + \rho\nabla\Phi$.

In the multidimensional case, in particular, this is the key for avoiding unbalanced approximations of projections of $\nabla p+\rho\nabla\Phi$ also in "horizontal" directions normal to $\nabla\Phi$.

As already mentioned, such approximations are constructed, in standard finite differences methods on terrain following coordinates, by summing up products between finite difference approximations of the partial derivatives of p along grid coordinates and metric coefficients. In the same methods, however, projections of $\rho\nabla\Phi$ in horizontal directions are set to zero i.e. they are computed exactly ! Virtually all numerical methods used in NWF are based on this separation of terms which are physically in balance. In fact, such methods require sophisticated (optimal) approximations, for instance of the metric terms, see [24], to enhance LTE cancellation.

In our approach this cancellation is obtained per construction. We *first* compute a numerical approximation to the sum $\nabla p+\rho\nabla\Phi$ with (7) and *then* project it in no matter what direction. As long as $P_i - P_i^{(0)}$ is of order ϵ, the LTE associated with any projection scales with ϵ. This holds independently of the quadrature rule used to approximate the integral on the right hand side of (7) or, in the finite difference parlance, for any consistent discretization of the metric terms.

The approach proposed here allows to accurately describe nearly hydrostatic flows by means of local operations. $P_i^{(0)}$, $R_i^{(0)}$ are cell functions that can be computed, usually analytically and at almost zero computational cost, on the basis of local data. This approach can be implemented with minimal modifications of the recovery stage of standard finite volume schemes. The implementation in existing standard finite difference methods is straightforward.

By avoiding the introduction of global approximations to $p^{(0)}$, $\rho^{(0)}$, the approach proposed here does not destroy the locality of the flux function of the Euler equations. This property is essential for constructing Godunov

type finite volume methods, whose built-in conservation properties make them promising candidates for climate applications. This class of schemes is considered in the present work.

In the next section we will analyze a one-dimensional standard central scheme and explain our strategy for controlling the LTE associated with $\nabla p + \rho\nabla\Phi$ in this simple framework. We also introduce the basic notation. In section 3 we extend these ideas and construct a class of second order well balanced Godunov type finite volume methods. In section 4 we discuss method validation criteria and present numerical results for a second order method in one and two space dimensions.

2. BALANCING IN THE CONTEXT OF CENTRAL FINITE DIFFERENCES

Let $q := \{\rho, \rho\boldsymbol{v}, \rho e\}$ be an exact solution of (1) for some initial and boundary conditions, a state equation φ and a gravity potential Φ. A semi-discrete time dependent numerical method for (1) is a rule

$$\frac{dQ_\omega}{dt} = A_\omega(Q_\omega, \Phi)$$

to advance a set $Q_\omega(t)$ of time dependent approximations to some functionals $q_\omega(t) := \delta_\omega(q(\cdot,t))$ of $q(\cdot,t)$. These may be the values of $q(\cdot,t)$ at some set of grid points $\omega = \boldsymbol{x} := \{\boldsymbol{x}_1, \ldots, \boldsymbol{x}_n\}$

$$\delta_{\boldsymbol{x}}(q(\cdot,t)) := \{\delta_{\boldsymbol{x}_1}(q(\cdot,t)), \ldots, \delta_{\boldsymbol{x}_n}(q(\cdot,t))\} \qquad \delta_{\boldsymbol{x}_i}(q(\cdot,t)) := q(\boldsymbol{x}_i, t)$$

as in finite difference methods, or the averages of q on grid cells $\omega = c := \{c_1, \ldots, c_n\}$

$$\delta_c(q(\cdot,t)) := \{\delta_{c_1}(q(\cdot,t)), \ldots, \delta_{c_n}(q(\cdot,t))\} \qquad \delta_{c_i}(q(\cdot,t)) := \frac{1}{|c_i|}\int\limits_{c_i} q(\boldsymbol{x},t)\, d\boldsymbol{x}$$

as in finite volume methods. The rule A_ω is written in terms of consistent approximations to the functionals of the differential operators appearing in (1). For the discussion to be developed here the dependence of q, q_ω, Q_ω, A_ω on the time t is nonessential. We therefore simplify the notation and neglect the dependency of these and other quantities on t for the rest of this section.

We have pointed out that standard approximations $G_\omega(Q_\omega)$, $S_\omega(Q_\omega, \Phi)$ to $\delta_\omega(\nabla p)$, $\delta_\omega(\rho\nabla\Phi)$ introduce local truncation errors even when applied to exact, nearly hydrostatic data $Q_\omega = q_\omega$. Furthermore, on finite grids these errors can be orders of magnitude larger than the true, order ϵ, acceleration. For example, in one space dimension and on a regular grid $x_i := ih$, $i = -\infty, \ldots, \infty$ and with exact, nearly hydrostatic data $p_{x_i} := \varphi(q(x_i))$,

$\rho_{x_i} := \rho(x_i)$, the approximation

$$G_{x_i} := \frac{p_{x_{i+1}} - p_{x_{i-1}}}{2h} \qquad S_{x_i} := -\rho_{x_i} \nabla\Phi(x_i) \tag{8}$$

leads, for sufficiently smooth data $\varphi(q)$, to

$$G_{x_i} - S_{x_i} = O(\epsilon) + \frac{1}{6}\frac{d^3\varphi}{dx^3}\bigg|_{x=x_i} h^2 + o(h^2)\,. \tag{9}$$

The $O(h^2)$ term clearly comes from the approximation of $\delta_{x_i}(dp/dx)$. In general, the problem of constructing well balanced approximations to $\delta_\omega(\nabla p)$, $\delta_\omega(\rho\nabla\Phi)$ can therefore be stated as follows

PROBLEM 2.1. *Given a nearly hydrostatic state q in the sense of (2), and discrete approximations Q_ω to q_ω with $Q_\omega = q_\omega + O(\epsilon h^r)$ on some grid of grid parameter h, find approximations $G_\omega(Q_\omega)$, $S_\omega(Q_\omega, \Phi)$ to $\delta_\omega(\nabla p)$ and $\delta_\omega(\rho\nabla\Phi)$ such that*

$$\lim_{\substack{\epsilon\to 0 \\ h=\text{const}}} (G_\omega - S_\omega) = 0\,. \tag{10}$$

This problem is difficult to solve in general and we will consider a particular case. Here we are not interested in solving the problem of reconstructing order ϵh^r approximations to q, $\varphi(q)$ from given order ϵh^r approximations to q_ω. The solution of this problem may be trivial or quite difficult depending on the order of accuracy r, on the functionals δ_ω, and on the functional form of φ, see [17].

We assume we are given exact point values $p_{\boldsymbol{x}} = \varphi(q(\boldsymbol{x}))$ of nearly hydrostatic data q. Under this assumption consider, in one space dimension and for each point x_i of a regular grid of grid spacing h, functions $P_i^{(0)}$, $R_i^{(0)}$ defined locally near x_i through

$$P_i^{(0)}, R_i^{(0)} \;:\quad \frac{dP_i^{(0)}}{dx} = -R_i^{(0)}\frac{d\Phi}{dx}, \quad P_i^{(0)}\big|_{x=x_i} = p_{x_i}\,,$$

with $P_i^{(0)}, R_i^{(0)}$ being coupled through some given distribution $\Theta_i^{(0)}$ of, e.g., the entropy (potential temperature) $\theta(p,\rho)$,

$$\theta(P_i^{(0)}(x), R_i^{(0)}(x)) = \Theta_i^{(0)}(x)\,.$$

Moreover, let

$$P_i(x) := P_i^{(0)}(x) + (x - x_i)\,\frac{\big(p_{x_{i+1}} - P_i^{(0)}(x_{i+1})\big) - \big(p_{x_{i-1}} - P_i^{(0)}(x_{i-1})\big)}{2h} \quad \forall x \in I\!R\,.$$

$P_i^{(0)}$ and $R_i^{(0)}$ depend on the initial condition p_{x_i} and on the functions θ and $\Theta_i^{(0)}$. $\Theta_i^{(0)}$ is an approximation to θ around x_i. The only constraint

we impose on $\Theta_i^{(0)}$ is that $\Theta_i^{(0)}(x_i) = \theta(p_{x_i}, \rho_{x_i})$. This constraint and the initial condition for $P_i^{(0)}$ guarantee that $P_i^{(0)}$, $R_i^{(0)}$ interpolate p, ρ at $x = x_i$, respectively. For simple choices of the thermodynamic variable θ and its local approximation $\Theta_i^{(0)}$, $P_i^{(0)}$ and $R_i^{(0)}$ can be computed analytically at virtual zero computational cost. With $P_i^{(0)}$ and P_i one can construct, for each point x_i, the following "balanced" approximations to $\delta_{x_i}(dp/dx)$ and $\delta_{x_i}(\rho d\Phi/dx)$

$$G^b_{x_i} := \frac{P_i(x_{i+1}) - P_i(x_{i-1})}{2h} \qquad S^b_{x_i} := -\frac{1}{2h}\int_{x_{i-1}}^{x_{i+1}} R_i^{(0)}(x)\frac{d\Phi}{dx}(x)\,dx \quad (11)$$

Notice that, per construction, $2hS^b_{x_i} = P_i^{(0)}(x_{i+1}) - P_i^{(0)}(x_{i-1})$ i.e. $\delta_{x_i}(\rho d\Phi/dx)$ has been approximated via the discrete Archimedes' buoyancy principle sketched in the introduction. Notice also that $G^b_{x_i}$ and $S^b_{x_i}$ are second order approximations to dp/dx and $\rho d\Phi/dx$ at $x = x_i$ in the standard sense. In particular, $G^b_{x_i} = G_{x_i}$ (see (8), left) and the local truncation error associated with this operator does not scale with ϵ. One has

$$\begin{aligned} G^b_{x_i} - S^b_{x_i} &= \frac{\left(p_{x_{i+1}} - P_i^{(0)}(x_{i+1})\right) - \left(p_{x_{i-1}} - P_i^{(0)}(x_{i-1})\right)}{2h} \\ &= O(\epsilon) + \sum_{k=1}^{\infty} \frac{1}{(2k+1)!}\left(\left.\frac{d^{2k+1}\varphi}{dx^{2k+1}}\right|_{x=x_i} - \left.\frac{d^{2k+1}P^{(0)}}{dx^{2k+1}}\right|_{x=x_i}\right) h^{2k}\,. \end{aligned} \quad (12)$$

As in (9), the error associated with the approximation of $dp/dx + \rho d\Phi/dx$ at $x = x_i$ depends on the grid parameter h. Here, however, we have control over this error. First of all notice that, for all $P_i^{(0)}$, $R_i^{(0)}$ constructed with the *exact* θ-distribution, i.e., with $\Theta_i^{(0)}(x) = \theta(p(x), \rho(x))$ one has

$$\left.\frac{d^{2k+1}\varphi}{dx^{2k+1}}\right|_{x=x_i} - \left.\frac{d^{2k+1}P^{(0)}}{dx^{2k+1}}\right|_{x=x_i} = O(\epsilon)\,,$$

and the scheme is well balanced. Of course this distribution is not known exactly in general but must itself be approximated discretely. In this case one can still control the balancing error by constructing higher order accurate approximations to θ, e.g., by means of polynomial reconstructions. Equation (12) also shows that $G^b_{x_i}$, $S^b_{x_i}$ are well balanced for all $p = \varphi(q)$, ρ such that $d\theta/dx, d\Theta_i^{(0)}/dx = O(\epsilon)$. This is a realistic scenario corroborated by non-dimensionalizations of a typical Brunt-Väisälä-frequency (buoyancy-frequency) of $N \sim 10^{-2}\,\mathrm{s}^{-1}$, e.g., in [23, 33]. The authors show that this order of magnitude for N is equivalent with small relative entropy variations of order $\delta\theta/\theta \sim 10^{-1}$. The special case of a homentropic atmosphere with

$\Theta_i^{(0)}$ chosen so that $\theta(p(x), \rho(x)) = \Theta_i^{(0)}(x) \equiv \text{const}$ suggests itself as a crucial analytical test case for validating our numerical approach and, up to a certain extent, its implementation, see section 4.

As mentioned in the introduction we cannot, at this stage, propose a method which is well balanced for *arbitrary* nearly hydrostatic initial data. However we have characterized classes of solutions for which our approach does yield well balanced approximations and we have argued that these solutions are relevant for typical atmospheric motions. For nearly hydrostatic flows not belonging to these classes of solutions improved balancing properties can still be achieved by increasing the accuracy of the approximation of a single scalar variable, such as the entropy or potential temperature. In the next section we apply this approach to construct well balanced finite volume methods in conservation form.

3. WELL BALANCED GODUNOV TYPE FINITE VOLUME METHODS

Finite volume Godunov type methods for (1) are rules to compute numerical approximations $Q_c(t)$ to the averages $\delta_c(q(\cdot,t))$ of $q(\cdot,t)$ on some set of grid cells c. For the purpose of constructing well balanced finite volume methods we only need to consider semi-discrete time dependent rules. In one space dimension and on a regular grid $x_i := ih$, $i = -\infty, \ldots, \infty$, these have the form:

$$\begin{aligned} -h\frac{d}{dt}Q_{c_i}(t) \;=\; & F\left(Q_i(x_i + h/2, t), Q_{i+1}(x_i + h/2, t), \Phi(x_i + h/2)\right) \\ & - \; F\left(Q_{i-1}(x_i - h/2, t), Q_i(x_i - h/2, t), \Phi(x_i - h/2)\right) \\ & - S_{c_i}(Q_c, \Phi)\,. \end{aligned} \tag{13}$$

$Q_{c_i}(t)$ is a numerical approximation to $\delta_{c_i}(q(\cdot,t))$, the average of q on $(x_i - h/2, x_i + h/2)$. F is a numerical flux consistent with the flux function of (1):

$$F(q, q, \Phi) = f(q, \Phi) \qquad f(q, \Phi) := \begin{pmatrix} \rho v \\ \rho v^2 + p \\ (\rho e + p + \rho\Phi)v \end{pmatrix}$$

$S_{c_i}(Q_c, \Phi)$ is a consistent approximation to the integral of the right hand side of (1) over c_i. Equipped with a quadrature rule for time integration and with some initial cell average, (13) yields finite volume methods in conservation form. The function $Q_i(\cdot,t)$ is an approximation to the exact solution $q(\cdot,t)$ on the i-th cell c_i. Let $Q(\cdot,t)$ be the relation obtained by piecing together all local approximations $Q_i(\cdot,t)$ i.e. $\forall x \in I\!R$

$$Q(x,t) := Q_i(x,t) \quad \text{for} \quad x \in [x_i - h/2, x_i + h/2]\,.$$

For the rest of this section we will simplify the notation and drop the dependency of all quantities on time. Q is reconstructed from the approximate cell averages Q_c. In standard methods it is a piecewise polynomial function of degree one or two, see, e.g., [30]. On each cell, degree one approximations to q can be easily constructed by localizing the cell averages in the cell centers and adding an approximation to dq/dx in the cell centers to the localized values. This approximation is usually computed by comparing neighboring finite differences through a limiting function $\mathcal{L}$

$$Q_i(x) := Q_{c_i} + (x - x_i)\,\mathcal{L}\left(\frac{Q_{c_i} - Q_{c_{i-1}}}{h}, \frac{Q_{c_{i+1}} - Q_{c_i}}{h}\right) \qquad \forall x \in I\!R\,. \tag{14}$$

$\mathcal{L}$ is constructed for Q to satisfy two conditions. The first condition requires Q to be a second order approximation to q for smooth exact data $Q_c = \delta_c(q)$. The second condition requires the total variation of Q to be less or equal to the total variation of Q_c in order to avoid spurious oscillations in the vicinity of sharp transitions, see [30].

In the previous section we have seen how to construct well balanced approximations to the grid point values of $dp/dx + \rho d\Phi/dx$ from given exact grid point values of $p = \varphi(q)$ and ρ. The task proved to be particularly straight-forward for homentropic and weakly stratified data. The approach consisted of 3 steps: first compute hydrostatically balanced local approximations $P_i^{(0)}$, $R_i^{(0)}$ to the hydrostatic components $p^{(0)}$, $\rho^{(0)}$ of $p = \varphi(q)$ and ρ. Second, construct local approximations P_i to p by adding linear approximations of $p - p^{(0)}$ to $P_i^{(0)}$. Third, given linear functionals $G^b_{x_i}$, construct consistent discretizations $S^b_{x_i}$ of the source term which exactly balance the hydrostatic components $G^b_{x_i}(P_i^{(0)})$. The keys for constructing $S^b_{x_i}$ were the hydrostatic relationship between $P^{(0)}$ and $R^{(0)}$ imposed in step 1 per construction *and* the linearity of $G^b_{x_i}$.

This construction can be extended to Godunov type finite volume methods by replacing standard piecewise polynomial reconstructions with functions involving the local approximations $P_i^{(0)}$, $R_i^{(0)}$ in analogy with the derivations in the previous section. There is a caveat, however. In Godunov type methods the discrete pressure gradient is not a stand alone quantity. It is a component of the discrete flux divergence appearing on the right hand side of (13). The flux divergence depends, through the numerical flux function, both on the interface values of Q_i *and* of Q_{i-1} and Q_{i+1}. We can still apply the 3-tier approach of section 2 but we must be able to ensure that, in the limit of exactly hydrostatic data, Q is continuous through cell interfaces. If this condition is not satisfied the approximate flux divergence will depend both on Q_i and, through the numerical flux function, on Q_{i-1} and Q_{i+1} in a non-trivial and non-linear fashion. In this case it is of course still possible to apply

the discrete Archimedes' principle to construct a consistent discretization of the source term in gradient form. This discretization, however, will not, in general, balance the flux divergence.

On the other hand, continuity of Q *and* consistency of the numerical flux function allow for the pressure gradient component of the discrete flux divergence to be expressed explicitly: Let $x_{i\pm} := x_i \pm h/2$, and let $F_{\rho v}$, $f_{\rho v}$ denote the ρv components of the approximate and exact flux functions F and f, respectively. Then the continuity conditions

$$Q_{i-1}(x_{i-}) = Q_i(x_{i-})\,, \qquad Q_i(x_{i+}) = Q_{i+1}(x_{i+})$$

imply

$$\begin{aligned}\Delta F_{\rho v,i} &:= F_{\rho v}\left(Q_i(x_{i+}), Q_{i+1}(x_{i+}), \Phi(x_{i+})\right) - F_{\rho v}\left(Q_{i-1}(x_{i-}), Q_i(x_{i-}), \Phi(x_{i-})\right)\\ &= F_{\rho v}\left(Q_i(x_{i+}), Q_i(x_{i+}), \Phi(x_{i+})\right) - F_{\rho v}\left(Q_i(x_{i-}), Q_i(x_{i-}), \Phi(x_{i-})\right)\\ &= f_{\rho v}\left(Q_i(x_{i+}), \Phi(x_{i+})\right) - f_{\rho v}\left(Q_i(x_{i-}), \Phi(x_{i-})\right)\\ &= \varphi(Q_i(x_{i+})) - \varphi(Q_i(x_{i-})) + \rho v^2(Q_i(x_{i+})) - \rho v^2(Q_i(x_{i-}))\end{aligned} \tag{15}$$

This information is crucial for the subsequent construction of a consistent well balanced discretization in that we will require cell interface discontinuities of the reconstructed distributions, such as $Q_i(x_{i-}) - Q_{i-1}(x_{i-})$, to vanish sufficiently rapidly as $\epsilon \to 0$.

Let $\mathcal{T}$ be the transformation which maps q to the so-called primitive variables u: density, velocity and pressure:

$$\mathcal{T}: \quad I\!R^N \ni q := \begin{pmatrix} \rho \\ \rho \boldsymbol{v} \\ \rho e \end{pmatrix} \quad \to \quad u = \mathcal{T}(q) := \begin{pmatrix} \rho \\ \rho \boldsymbol{v}/\rho \\ \varphi(q) \end{pmatrix} \in I\!R^N\,.$$

N is equal to 2 plus the number of space dimensions. For the one-dimensional finite volume method described above $N = 3$. We describe the construction of a well balanced finite volume method in this case. The extension to the multidimensional case and to the case in which the equations are augmented by some evolution equation for tracers, water vapor, or chemical species is straightforward, see algorithms 1 and 2 in the next section. Let $U_{c_i} = \{R_{c_i}, V_{c_i}, P_{c_i}\} = \mathcal{T}(Q_{c_i})$ denote the primitive variables associated with the approximate cell averages. As with Q_{c_i} we localize these values in the cell centers $\boldsymbol{x}_i$. This is consistent with second order accuracy. In this manuscript we stay within the framework of second order methods and use Q_{c_i} (and U_{c_i}, R_{c_i}, etc.) to denote both approximate cell averages and approximate cell center values. For the much more involved problem of recovering higher order point values from higher order cell averages see

[17]. On each cell, let $R_i^{(0)}$, $P_i^{(0)}$ be the functions computed in the previous section with initial values $P_i^{(0)}\big|_{x=x_i} = P_{c_i}$ and with $\Theta_i^{(0)}$ satisfying the interpolation condition $\Theta_i^{(0)}(x_i) = \theta(P_{c_i}, R_{c_i})$. Then $R_i^{(0)}$, $P_i^{(0)}$ interpolate R_{c_i}, P_{c_i} in $x = x_i$, respectively. Let also $V_i^{(0)}(x) := V_{c_i}\ \forall\, x \in I\!R$.

With $U_i^{(0)} := \{R_i^{(0)}, V_i^{(0)}, P_i^{(0)}\}$ one can construct a local approximation $Q_i^{(0)}$ to the hydrostatic component of q in each cell:

$$Q_i^{(0)}(x) := \mathcal{T}^{-1}\left(U_i^{(0)}(x)\right) \quad \forall x \in I\!R\,.$$

With $Q_i^{(0)}$ one can construct, again on each cell, the following local approximation to q

$$Q_i(x) := Q_i^{(0)}(x) + (x - x_i)\,\mathcal{L}\left(\frac{Q_i^{(0)}(x_{i-1}) - Q_{c_{i-1}}}{h}, \frac{Q_{c_{i+1}} - Q_i^{(0)}(x_{i+1})}{h}\right) \tag{16}$$

$\forall\, x \in I\!R$. Notice that, due to the interpolation properties imposed on $R_i^{(0)}$, $P_i^{(0)}$ and $V_i^{(0)}$, $Q_i^{(0)}(x_i) = Q_{c_i}$. Thus, the numerator of the first argument of $\mathcal{L}$ can be written as $\left(Q_{c_i} - Q_i^{(0)}(x_i)\right) - \left(Q_{c_{i-1}} - Q_i^{(0)}(x_{i-1})\right)$. Similarly, the numerator of the second arguments reads: $\left(Q_{c_{i+1}} - Q_i^{(0)}(x_{i+1})\right) - \left(Q_{c_i} - Q_i^{(0)}(x_i)\right)$. These expanded forms make clear that the arguments of $\mathcal{L}$ are one sided approximations to the slope of the *deviation* $q - q^{(0)}$ at $x = x_i$. We have not increased the order of accuracy of the standard reconstruction (14); $q - q^{(0)}$ is still approximated by piecewise linear functions. However, we have provided an improved representation of $q^{(0)}$ by introducing exact solutions of the hydrostatic relationship in the construction of Q_i. The last step is to define a balanced approximation for the source term $S_{c_i}(Q_c, \Phi)$. Similarly to the previous section we take

$$S_{c_i} := -\int_{x_{i-}}^{x_{i+}} R_i^{(0)}(x)\frac{d\Phi}{dx}(x)\,dx = \int_{x_{i-}}^{x_{i+}} \frac{dP_i^{(0)}}{dx}\,dx = P_i^{(0)}(x_{i+}) - P_i^{(0)}(x_{i-})\,. \tag{17}$$

Let us now consider the finite volume method (13) with Q_i, S_{c_i} defined according to (16) and (17), respectively. Q_i depends on the cell averages of a local neighborhood of c_i, say $n(c_i)$. In the one-dimensional case $n(c_i)$ is simply the set $\{c_{i-1}, c_i, c_{i+1}\}$. We say that c_i is in local hydrostatic balance with its neighborhood $n(c_i)$ if $Q_{c_j} = Q_i^{(0)}(x_j)\ \forall\ j : c_j \in n(c_i)$ i.e., if the localized neighboring cell averages lie on the local approximate hydrostatic manifold $Q_i^{(0)}$ of c_i (Q_{c_i} is always identical to $Q_i^{(0)}(x_i)$ per construction). In this case $Q_i \equiv Q_i^{(0)}$ because $\mathcal{L}(0,0)$ is always zero for consistency. Consider a set of cell averages Q_c in local hydrostatic balance i.e.

$$Q_c: \quad Q_{c_j} = Q_i^{(0)}(x_j) \quad \forall j : c_j \in n(c_i) \quad \forall i : c_i \in c\,.$$

Also, let the flow velocity be identically zero i.e. $v_{c_i} = 0 \; \forall \; c_i \in c$. Then, under suitable boundary conditions, we should expect Q_c to be exactly balanced and therefore a fixed point of (13). This is indeed the case, provided Q is continuous through cell interfaces. In this case (15) and (17) imply, together with $Q_i = Q_i^{(0)}$

$$\begin{aligned} -h\frac{d}{dt}Q_{c_i} &= \varphi(Q_i(x_{i+})) - \varphi(Q_i(x_{i-})) - \left(P_i^{(0)}(x_{i+}) - P_i^{(0)}(x_{i-})\right) \\ &= \varphi(Q_i^{(0)}(x_{i+})) - \varphi(Q_i^{(0)}(x_{i-})) - \left(P_i^{(0)}(x_{i+}) - P_i^{(0)}(x_{i-})\right) = 0 \end{aligned} \tag{18}$$

This analysis can be easily extended to the multidimensional case in which, in general, the acceleration of gravity $-\nabla\Phi$ is not aligned with any grid coordinate. In the x-z slice model shortly described in section 4, for instance, the neighborhood $n(c_{i,j})$ of an internal cell is the set $\{c_{i-1,j}, c_{i+1,j}, c_{i,j}, c_{i,j-1}, c_{i,j+1}\}$ and a multidimensional analogon of (18) can be easily derived. The continuity of Q implies some restrictions both on the classes of data for which the method can be exactly balanced and on the choice of the *entropy* functions used to construct $Q_i^{(0)}$. Notice that homentropic data Q_c : $\theta(\varphi(Q_c), \rho_c) = \text{const.}$ are, under the assumptions discussed above and for $\Theta_i^{(0)} = \theta(\varphi(Q_{c_i}), \rho_{c_i}) = \text{const.}$, exactly balanced.

Thus, homentropic, zero velocity initial data with suitable boundary conditions are a natural starting point for validating implementations of well balanced methods: a failure to preserve such initial data unmistakably indicates some implementation error. Homentropic, zero velocity initial data characterize the first case discussed in the next section.

The case of almost hydrostatic data cannot be analyzed as easily as in the finite difference case. The starting point here would be to estimate the second term on the right hand side of (16) in much the same way as done for the central finite difference in (12). One could then insert the result into the numerical flux function and use Lipschitz continuity to obtain an estimate for dQ_{c_i}/dt. We do not expand on this analysis here.

4. METHOD VALIDATION CRITERIA AND RESULTS

In the previous section we have proposed a strategy for constructing well balanced Godunov type finite volume methods. We have avoided specifying important components of the method – among others the time discretization, the limiting function $\mathcal{L}$, the numerical flux F and the state equation φ – and suggested that any standard method defined in terms of these components can be modified to survive the hydrostatic limit by simply replacing recovery and source term discretization.

Of course, we have, either implicitly or explicitly, required $\mathcal{L}$, F, φ and, in general, the standard method to satisfy some reasonable assumptions. Under

these assumptions, e.g., consistency of the numerical flux, we have shown in section 3 that zero velocity, hydrostatically balanced homentropic data are, for $\Theta_i^{(0)} = \theta(\varphi(Q_{c_i}), \rho_{c_i})$, stationary solutions of the modified method (13), (16) and (17). Thus, we have identified a class of discrete solutions for which the modified method is exactly balanced. Ideally we would like to show that, again under reasonable assumptions, any standard method, when modified according to our strategy,

- is well balanced in that initial data satisfying (2) generate order ϵ accelerations independently of the grid size, h,
- converges, and
- is second order accurate.

Moreover, it would be desirable to construct particular well balanced methods which yield accurate results for standard benchmark problems, as described, e.g., in [3], [36], [20], [40], [21].

In this section we give some numerical evidence that, at least for a particular method, these goals are achieved. We start with a specification of the concrete method we have implemented for simulating the flow of a calorically perfect gas. The equation of state used below reads

$$\varphi(q) = \varphi(\rho, \rho\boldsymbol{v}, \rho e) := (\gamma - 1)(\rho e - 1/2\rho\boldsymbol{v}\cdot\boldsymbol{v})$$

with $\gamma = 1.4$. $\nabla\Phi$ is taken to be constant and equal to $g\boldsymbol{k}$ where g is the acceleration of gravity and $\boldsymbol{k}$ is one of the unit basis vectors of a Cartesian frame of reference. Two dimensional computations have been done on a curvilinear grid fitted to the bottom topography. In all computations we have used uniform spacing both in the horizontal and in the vertical direction, the latter being that oriented in the direction of $\boldsymbol{k}$. This means that, in a two dimensional domain

$$I\!R^2 \supset \Omega := \left\{x^1, x^2 : x^1 \in [a, b], x^2 \in [z_{\rm b}(x^1), z_{\rm t}(x^1)]\right\}$$

between some bottom topography $x^2 = z_{\rm b}(x^1)$ and some upper boundary $x^2 = z_{\rm t}(x^1)$ the coordinates $x^1_{i,j}$, $x^2_{i,j}$ of the i, j-th grid point are

$$\begin{aligned} x^1_{i,j} &:= x^1_i = a + i\,(b-a)/(n_1 - 1) \\ x^2_{i,j} &:= z_{\rm b}(x^1_i) + j\,\left(z_{\rm t}(x^1_i) - z_{\rm b}(x^1_i)\right)/(n_2 - 1) \end{aligned}$$

for $i \in I_n$, $j \in J_n$ with I_n and J_n one-dimensional index ranges. The finite volumes $c_{i,j} \in c$ have been constructed by connecting the grid points by means of straight line segments. In all cell centers, we assume that a mapping $\mathcal{J}$ from a computational space $\boldsymbol{y} := \{y^1, y^2\}$ into the physical space $\boldsymbol{x} := \{x^1, x^2\}$ exists, is regular and such that:

$$y^k = (\mathcal{J}^{-1}(\boldsymbol{x}_{i,j}))^k = \begin{cases} i & \text{if} \quad k = 1\,, \\ j & \text{if} \quad k = 2\,. \end{cases}$$

Time integration is done with the standard 2 step Runge-Kutta method. The maximal time step $\Delta t^{\max}$ is estimated as follows

$$\Delta t^{\max} := \min_{\omega \in c} \left(\sum_{k=1}^{2} \frac{1}{\Delta t^{\max}_{\omega,k}} \right)^{-1}, \qquad \Delta t^{\max}_{\omega,k} := \min \left(\Delta t^{\max}_{\omega,k-}, \Delta t^{\max}_{\omega,k+} \right) .$$

$\Delta t^{\max}_{\omega,k}$ is the maximal time step which can be used for an explicit update of ω based on the fluxes through the interfaces, $\partial\omega_{k-}$ and $\partial\omega_{k+}$ crossed by the k-th coordinate lines. For $\omega = c_{m,n}$, for instance, $\partial\omega_{1\pm} = c_{m,n} \cap c_{m\pm1,n}$ and $\partial\omega_{2\pm} = c_{m,n} \cap c_{m,n\pm1}$. $\Delta t^{\max}_{\omega,k-}$ and $\Delta t^{\max}_{\omega,k+}$ are computed according to the following CFL rules, [38]:

$$\Delta t^{\max}_{\omega,k\pm} := \frac{\pm|\,\omega\,|}{|\partial\omega_{k\pm}| \max\limits_{p} \left(\lambda_p(Q_{\omega_{k\pm}}, \boldsymbol{n}|_{\partial\omega_{k\pm}}), \lambda_p(Q_\omega, \boldsymbol{n}|_{\partial\omega_{k\pm}}), 0 \right)}$$

where $|\omega|$ is the area of ω and $|\partial\omega_{k-}|$, $|\partial\omega_{k+}|$ are the lengths of $\partial\omega_{k-}$ and $\partial\omega_{k+}$, respectively. ω_{k-} and ω_{k+} are those neighboring cells of ω which share the interfaces $\partial\omega_{k-}$ and $\partial\omega_{k+}$ with ω. $\lambda_p(q, \boldsymbol{n})$ are the eigenvalues of the Jacobian of the flux function of the Euler equations

$$f(q, \boldsymbol{n}) := \begin{pmatrix} \rho \boldsymbol{v} \cdot \boldsymbol{n} \\ \rho \boldsymbol{v} \boldsymbol{v} \cdot \boldsymbol{n} + p \boldsymbol{n} \\ (\rho e + p) \boldsymbol{v} \cdot \boldsymbol{n} \end{pmatrix}$$

of (1). $\boldsymbol{n}|_{\partial\omega_{k-}}$, $\boldsymbol{n}|_{\partial\omega_{k+}}$ are unit vectors normal to $\partial\omega_{k-}$, $\partial\omega_{k+}$, respectively, both oriented in the increasing direction of the k-th coordinate. All computations have been done with $\Delta t = 0.8\Delta t^{\max}$. On each finite volume $c_{i,j} \in c$, the functions $Q^{(0)}_{i,j}$, $Q_{i,j}$ are reconstructed from the approximate cell averages Q_c and evaluated, at fixed discrete times and in the mid-points $\boldsymbol{x}_{i\pm,j}$ and $\boldsymbol{x}_{i,j\pm}$ of the interfaces between $c_{i,j}$ and $c_{i\pm1,j}$, $c_{i,j\pm1}$, respectively, according to *Algorithm 1*.

As mentioned in section 2, step 2 of algorithm 1 can be improved by means of more accurate local approximations of entropy. All computations presented in this section have been done with piecewise constant entropy profiles: $P^{(0)}_{i,j}/{R^{(0)}_{i,j}}^{\gamma} = \varphi(Q_{c_{i,j}})/R^{\gamma}_{c_{i,j}}$.

Notice that different approximations to $\nabla(q - q^{(0)})$, $G_i \delta Q_{i,j}$ and $G_j \delta Q_{i,j}$, are used in the evaluation of $Q_{i,j}$ at cell interfaces crossed by the first and by the second coordinate lines, respectively. In the computation of these approximate gradients the metric terms $\partial y^l/\partial x^m$ have been computed by inverting the Jacobian matrix of $\mathcal{J}$. The limiting function $\mathcal{L}$ is the monotonized central limiter, see [26], [42]. For scalar arguments a and b

Algorithm 1 2d: interface mid-point recovery

1: **for all** $i, j : i \in I_c, j \in J_c$ **do**

2: Compute $U^{(0)}_{i,j}(\xi) := \{R^{(0)}_{i,j}(\xi), \boldsymbol{V}^{(0)}_{i,j}(\xi), P^{(0)}_{i,j}(\xi)\}$ with $R^{(0)}_{i,j}(\xi)$, $P^{(0)}_{i,j}(\xi)$ such that

$$\frac{dP^{(0)}_{i,j}}{d\xi} = -R^{(0)}_{i,j} g\,, \quad P^{(0)}_{i,j}(0) = \varphi(Q_{c_{i,j}})\,, \quad P^{(0)}_{i,j}/{R^{(0)}_{i,j}}^{\gamma} = \varphi(Q_{c_{i,j}})/R^{\gamma}_{c_{i,j}}\,,$$

and $\boldsymbol{V}^{(0)}_{i,j} = \boldsymbol{V}_{c_{i,j}}$.

3: Compute the (vertical) distances $\xi_{i\pm1,j}$, $\xi_{i,j\pm1}$ of the neighbor cell centers $\boldsymbol{x}_{i\pm1,j}$, $\boldsymbol{x}_{i,j\pm1}$ of $c_{i,j}$ from the normal to $\boldsymbol{k}$ passing through $x_{i,j}$.

4: Evaluate $Q^{(0)}_{i,j} := \mathcal{T}^{-1}(U^{(0)}_{i,j})$ in the cell centers $\boldsymbol{x}_{i\pm1,j}$ and compute the deviation between neighboring localized approximate cell averages and the these values:

$$\delta Q_{i\pm1,j} := Q_{c_{i\pm1,j}} - Q^{(0)}_{i,j}(\xi_{i\pm1,j})\,, \qquad \delta Q_{i,j\pm1} := Q_{c_{i,j\pm1}} - Q^{(0)}_{i,j}(\xi_{i,j\pm1})$$

5: **for** $k = 1$ to 2 **do**

6: Compute *left* and *right* approximations to the gradient of $q - q^{(0)}$ in $c_{i,j}$

$$G\delta Q^k_{i\pm,j} := \delta Q_{i\pm1,j}\frac{\partial y^1}{\partial x^k} + \frac{1}{4}\left(\delta Q_{i,j+1} - \delta Q_{i,j-1} + \delta Q_{i\pm1,j+1} - \delta Q_{i\pm1,j-1}\right)\frac{\partial y^2}{\partial x^k}$$
$$G\delta Q^k_{i,j\pm} := \frac{1}{4}\left(\delta Q_{i+1,j} - \delta Q_{i-1,j} + \delta Q_{i+1,j\pm1} - \delta Q_{i-1,j\pm1}\right)\frac{\partial y^1}{\partial x^k} + \delta Q_{i,j\pm1}\frac{\partial y^2}{\partial x^k}$$

7: Compute *limited* approximations to the gradient of $q - q^{(0)}$ in $c_{i,j}$

$$G_i\delta Q^k_{i,j} := \mathcal{L}\left(G\delta Q^k_{i-,j}, G\delta Q^k_{i+,j}\right)\,, \qquad G_j\delta Q^k_{i,j} := \mathcal{L}\left(G\delta Q^k_{i,j-}, G\delta Q^k_{i,j+}\right)$$

8: **end for**

9: Evaluate $Q_{i,j}$ at the mid-points $\boldsymbol{x}_{i\pm,j}$, $\boldsymbol{x}_{i,j\pm}$ of the interfaces between $c_{i,j}$ and its neighborhood:

$$Q_{i,j}(\boldsymbol{x}_{i\pm,j}) = Q^{(0)}_{i,j}(\boldsymbol{x}_{i\pm,j}) + (\boldsymbol{x}_{i\pm,j} - \boldsymbol{x}_{i,j}) \cdot G_i\delta Q_{i,j}$$
$$Q_{i,j}(\boldsymbol{x}_{i,j\pm}) = Q^{(0)}_{i,j}(\boldsymbol{x}_{i,j\pm}) + (\boldsymbol{x}_{i,j\pm} - \boldsymbol{x}_{i,j}) \cdot G_j\delta Q_{i,j}$$

10: **end for**

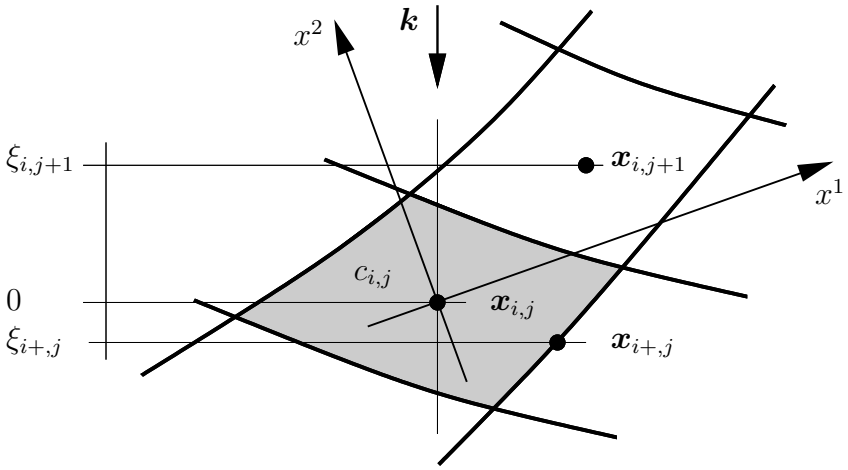

FIG. 2. Control volume $c_{i,j}$, "vertical" direction $\boldsymbol{k}$, Cartesian frame of reference (x^1, x^2), coordinate directions and distance functions.

this function is

$$\mathcal{L}(a,b) := \begin{cases} 0 & \text{if } ab \leq 0, \\ \dfrac{a}{|a|} \min\left(2\min(|a|,|b|), \dfrac{|a+b|}{2}\right) & \text{if } ab > 0. \end{cases}$$

Whenever $\mathcal{L}$ has been applied to non-scalar arguments the above function has been applied componentwise. We have modified the numerical flux proposed by Einfeldt in [12] to account for the potential energy term as follows. Let F^E_ρ, $F^E_{\rho\boldsymbol{v}}$ and $F^E_{\rho e}$ be the components of Einfeldt's numerical flux for the Euler equations i.e. (1) with $\Phi = 0$. The numerical flux we have used for the full equations is simply $F := \{F^E_\rho, F^E_{\rho\boldsymbol{v}}, F^E_{\rho e} + F^E_\rho \Phi\}$. Since the original numerical flux is consistent with the Euler equations the modified numerical flux is consistent with (1).

Consistently with the approach outlined in the introduction and with the analysis presented in section 3 for the one-dimensional case, the source term has been computed with algorithm 2.

Notice that, in spite of the fact that we are actually using a grid in which one family of coordinate lines are in fact straight lines parallel to $\boldsymbol{k}$, the algorithms sketched above do not rely on this assumption and the method can be used on general curvilinear grids. Note also the correspondence between algorithm 1 and 2. It is this correspondence (together, as shown in section 3 for the one-dimensional case, with the continuity of the reconstruction across cell interfaces and with the consistency of the numerical flux) that guarantees that, for cell averages Q_c in local hydrostatic balance

$$Q_c: \quad Q_{c_{i,j}} = Q^{(0)}_{m,n}(x_{i,j}) \quad \forall i,j : c_{i,j} \in n(Q_{m,n}) \quad \forall m,n : c_{m,n} \in c\,,$$

Algorithm 2 2d: source term computation

1: **for all** $i, j : i \in I_c, j \in J_c$ **do**

2: Compute $U^{(0)}_{i,j}(\xi) := \{R^{(0)}_{i,j}(\xi), \boldsymbol{V}^{(0)}_{i,j}(\xi), P^{(0)}_{i,j}(\xi)\}$ with $R^{(0)}_{i,j}(\xi)$, $P^{(0)}_{i,j}(\xi)$ such that

$$\frac{dP^{(0)}_{i,j}}{d\xi} = -R^{(0)}_{i,j} g\,, \quad P^{(0)}_{i,j}(0) = \varphi(Q_{c_{i,j}})\,, \quad P^{(0)}_{i,j}/{R^{(0)}_{i,j}}^{\gamma} = \varphi(Q_{c_{i,j}})/R^{\gamma}_{c_{i,j}}\,,$$

and $\boldsymbol{V}^{(0)}_{i,j} = \boldsymbol{V}_{c_{i,j}}$.

3: Compute the (vertical) distances $\xi_{i\pm,j}$, $\xi_{i,j\pm}$ between the mid-points $\boldsymbol{x}_{i\pm,j}$, $\boldsymbol{x}_{i,j\pm}$ of the interfaces between $c_{i,j}$ and its neighborhood and the normal to $\boldsymbol{k}$ passing through $x_{i,j}$.

4: Evaluate $P^{(0)}_{i,j}$ at the mid-points $\boldsymbol{x}_{i\pm,j}$, $\boldsymbol{x}_{i,j\pm}$ of the interfaces between $c_{i,j}$ and its neighborhood and compute the approximate the source term

$$S_{c_{i,j}} := \frac{1}{|c_{i,j}|}\int\limits_{c_{i,j}} R^{(0)}_{i,j}\nabla\Phi\, dV = -\frac{1}{|c_{i,j}|}\oint\limits_{\partial c_{i,j}} P^{(0)}_{i,j}\,\boldsymbol{n}\, dS$$

with exactly the same quadrature rule which is used for computing the discrete flux divergence (from the interface mid-point values recovered as in algorithm 1).

5: **end for**

the discrete flux divergence constructed with the mid-point values $Q_{i,j}(\boldsymbol{x}_{i\pm,j})$, $Q_{i,j}(\boldsymbol{x}_{i,j\pm})$ computed in algorithm 1 exactly balances the source term of algorithm 2 leading thus to exact zero tendencies.

4.1. Method implementation and stability

Here we check our implementation by considering the almost trivial test case of a hydrostatically balanced atmosphere at rest over non-vanishing topographical elevations. The numerical experiment is designed to show that the implementation does not fail to reproduce stationary solutions for zero velocity, hydrostatically balanced homentropic data. As shown in section 3 for the one-dimensional case and explained in the introduction and in the previous paragraphs for the multidimensional case, this is a property of the method. There is a caveat, however. When a discrete method is mapped into some implementation one cannot expect properties like the one we want to check to hold *exactly*. This issue arises because we are bound to operate with finite precision machine arithmetics. Therefore, implementations of equation (18) will generally not yield an exact balance but accelerations of the order of the round-off error. Since the first two terms on the right hand side of (18) are computed by different sequences of operations than the last two terms of the same equation, this true even for initial data which are exactly representable in the available set of machine numbers.

At risk of stating the obvious let us stress that these tendencies have nothing to do with the local truncation errors of the discretization which, for the class of data considered, has been proven to be exactly balanced. On an infinite precision machine these errors would disappear whereas the LTEs of any discretization would not.

An interesting question which is closely related with important properties of the method – stability and dissipativity – is that of the fate of such perturbations. How will they evolve in time? The continuous problem has no dissipation mechanism and there is no background flow to transport perturbations downwind and advect undisturbed fields into the physical domain. The original discrete method has some built-in dissipation in the form of local truncation errors, and for sufficiently small time steps we expect the LTEs of the balanced scheme to also have the structure of some grid dependent dissipation. On the other hand, it is exactly the local truncation errors which we are influencing by our balancing technique.

Thus, it is interesting not only to assess the smallness of initial accelerations but to investigate the time evolution of these perturbations on time scales comparable with those of realistic simulations. Two such evolutions are represented on the right of figure 3 for the maximum norm of the vertical velocity. The two curves correspond to computations in double and single precision. Time is measured in days and vertical velocity in meters per second. Both computations have been done on the grid shown on the left of

figure 3 where the units of length are kilometers. The initial cell averages are the cell center values of a homentropic atmosphere at rest. This is defined by the following functions of the vertical coordinate z:

$$p(z) = p_0^{-\frac{1}{\gamma-1}} \left(p_0 - \frac{\gamma-1}{\gamma} g\rho_0 z \right)^{\frac{\gamma}{\gamma-1}}$$

$$\rho(z) = \rho_0 \left(\frac{p(z)}{p_0} \right)^{\frac{1}{\gamma}}, \qquad \rho_0 = \frac{p_0}{RT_0}$$

$\forall\ z \in [0, 8]$ km and with p_0, T_0, g and R equal to 10^5 Nm^{-2}, 288.15 °K, 10 ms^{-2} and 287 $\mathrm{NmKg}^{-1}\mathrm{°K}^{-1}$, respectively. On the bottom boundary the condition $\boldsymbol{v}\cdot\boldsymbol{n} = 0$ has been imposed on the numerical flux by computing, for any given inner state $q := \{\rho, \rho\boldsymbol{v}, \rho e\}$ and any unit normal vector $\boldsymbol{n}$, the "reflected" outer state $q_o =: \{\rho, \rho\mathcal{R}(\boldsymbol{v}, \boldsymbol{n}), \rho e\}$ with $\mathcal{R}(\boldsymbol{v}, \boldsymbol{n}) := \boldsymbol{v} - 2(\boldsymbol{v}\cdot\boldsymbol{n})\boldsymbol{n}$. On the other boundaries the outer state is fixed to its initial value. The grid consists of 64 cells in the horizontal direction and 32 cells in the vertical direction on a 16×8 km computational domain. Thus, all cells have a width of 250 m. The vertical cell size ranges from about 190 m over the top of the mountain and 250 m on the sides of the domain.

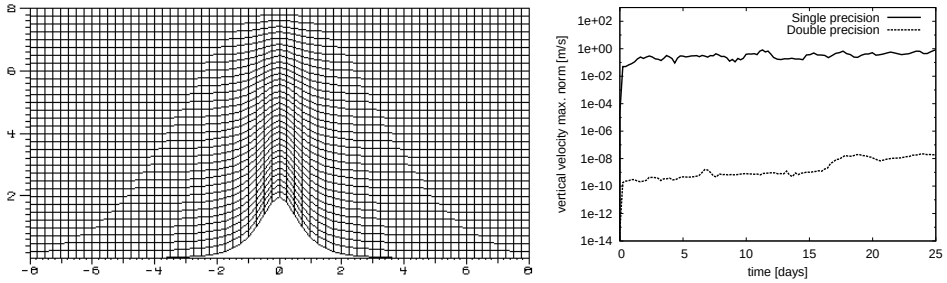

FIG. 3. Hydrostatic homentropic flow at rest above steep topography. Left: computational domain (km) and finite volumes grid (64×32). Right: vertical velocity maximum norm (ms^{-1}) versus time (days).

The time step was fixed to 0.2 sec throughout the computation. In the numerical results show in figure 3, attention is focused on the dynamics at large times. A picture of the maximal vertical velocity at short times would show that, during an initial time interval covered by about 300 steps, the tendencies are, indeed, of the order of magnitude of the round-off error, see 4.2. After an initial growth, the maximal vertical velocity stabilizes around values of about 1 and 10^{-8} ms^{-1} for single and double precision, respectively. Notice that 10^{-8} is about twenty times the ratio between `DBL_EPSILON` and `FLT_EPSILON` (in our architecture equal to 2.2204460492503131e-16 and 1.19209290e-07F, respectively).

4.2. Smooth stratification and inversion: balancing properties

We first investigate the behavior of the well balanced scheme for smoothly stratified initial data. As in the previous case, the atmosphere is in hydrostatic balance at rest but the variable χ, which is closely related to the thermodynamic entropy or to the potential temperature, is a linear function of the vertical coordinate z:

$$\chi := \alpha^2 \frac{p}{\rho^\gamma} = \alpha^2 \frac{p_0}{\rho_0^\gamma} (1 + \sigma z) \ , \qquad \alpha := \frac{2}{\gamma - 1} \, .$$

This leads to the following distributions of initial pressure and density

$$p(z) = p_0 \left(p_0 - \frac{1}{\sigma} g \rho_0 \left((1 + \sigma z)^{\frac{\gamma-1}{\gamma}} - 1 \right) \right)^{\frac{\gamma}{\gamma-1}}$$

$$\rho(z) = \rho_0 \left(\frac{p(z)}{p_0} \frac{1}{1 + \sigma z} \right)^{\frac{1}{\gamma}} \ , \qquad \rho_0 = \frac{p_0}{R T_0}$$

$\forall \ z \in [0, 8]$ km. The values for p_0, T_0, g, and R are chosen as in the previous experiment. In figure 4 we have reported the time evolution of the maximum norm of the vertical velocity for σ equal to $1.2 \cdot 10^{-6}$, $1.2 \cdot 10^{-5}$ and $1.2 \cdot 10^{-4}$ m^{-1} and on two different grids. Time is given in minutes and vertical velocity in meters per second. The rougher grid is the same used in the previous experiment. The finer grid has twice as many cells in both directions. The case $\sigma = 1.2 \cdot 10^{-5}$ m^{-1} corresponds to a lapse rate of 0.0075 degrees per meter (0.0065 degrees per meter is the lapse rate of a standard atmosphere). The value $\sigma = 1.2 \cdot 10^{-4}$ m^{-1} corresponds to an unrealistically strongly stratified atmosphere in which the temperature increases with altitude at a rate of about 0.01 degrees per meter.

According to the analysis discussed in section 2, the local truncation errors associated with the discretization of the difference between pressure gradient and weight vertical velocities should scale with σ times the square of the grid parameter. Thus we expect the vertical velocity to behave in much the same way. Figure 4 shows that, at least at short times, this is indeed the case.

In order to assess the behavior of our balancing approach for more realistic stratifications, we consider the case of an atmosphere with a stable layer intersecting the topography. Geometry and discretizations are the same as in the previous experiment, see also figure 3. The layer is located between z_b and z_a. Inside this layer the buoyancy frequency

$$N := \sqrt{-g \left(\frac{1}{\rho} \frac{\partial \rho}{\partial z} + g \frac{\rho}{\gamma p} \right)} \tag{19}$$

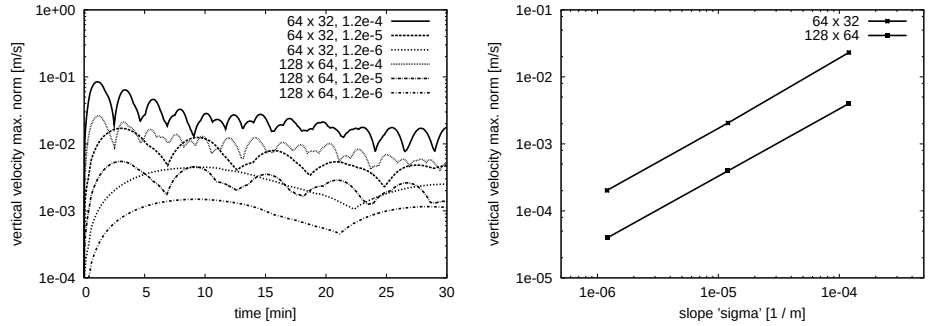

FIG. 4. Hydrostatic flow with linear entropy distribution at rest above steep topography. Left: Vertical velocity maximum norm (ms^{-1}) versus time (minutes) for σ equal to $1.2 \cdot 10^{-6}$, $1.2 \cdot 10^{-5}$ and $1.2 \cdot 10^{-4}$ m^{-1} and 64×32 and 128×64 finite volumes grids. Right: Vertical velocity maximum norm (ms^{-1}) after 1 minute versus σ (m^{-1}): 64×32 and 128×64 grids.

is constant and equal to $N_0 + \Delta N$. Above and below this layer N is equal to N_0.

The values of z_b, z_a are 750 and 1250 m, respectively i.e. the layer is centered at a height of one kilometer and is 500 m deep. The mountain top is at 2 kilometers. We consider three cases with $N_0 = 0.01$ s^{-1} and ΔN equal to 0, 0.005 and 0.01 s^{-1} and a fourth case in which N is constant and equal to 0.02 s^{-1}. The third case corresponds to an inversion in which the temperature increases with the altitude at a rate of about 0.0014 degrees per meter. The values for p_0, T_0, g, and R are chosen as in the previous experiment. The vertical profiles of pressure, density and temperature are

$$p(z),\ \rho(z) = \begin{cases} p_b(z),\ \rho_b(z) & \text{for} \quad z \le z_b \\ p_l(z),\ \rho_l(z) & \text{for} \quad z_b < z \le z_a \\ p_a(z),\ \rho_a(z) & \text{for } z_b < z \end{cases} \qquad T(z) = \frac{p(z)}{R\rho(z)}$$

$$p_b(z) = p_0 \left(1 - \frac{\gamma-1}{\gamma}\frac{1}{RT_0}\frac{g^2}{N_0^2}\left(1 - \exp\left(-\frac{N_0^2}{g}z\right)\right)\right)^{\frac{\gamma}{\gamma-1}}$$

$$p_l(z) = p_b(z_b) \left(1 - \frac{\gamma-1}{\gamma}\frac{1}{RT(z_b)}\frac{g^2}{(N_0+\Delta N)^2}\left(1 - \exp\left(-\frac{(N_0+\Delta N)^2}{g}(z-z_b)\right)\right)\right)^{\frac{\gamma}{\gamma-1}}$$

$$p_a(z) = p_l(z_a) \left(1 - \frac{\gamma-1}{\gamma}\frac{1}{RT(z_a)}\frac{g^2}{N_0^2}\left(1 - \exp\left(-\frac{N_0^2}{g}(z-z_a)\right)\right)\right)^{\frac{\gamma}{\gamma-1}}$$

$$\rho_b(z) = \rho_0 \left(\frac{p_b(z)}{p_0}\right)^{\frac{1}{\gamma}} \exp\left(-\frac{N_0^2}{g}z\right)$$

$$\rho_l(z) = \rho_b(z_b) \left(\frac{p_l(z)}{p_b(z_b)}\right)^{\frac{1}{\gamma}} \exp\left(-\frac{(N_0+\Delta N)^2}{g}(z-z_b)\right)$$

$$\rho_a(z) = \rho_l(z_a) \left(\frac{p_a(z)}{p_l(z_a)}\right)^{\frac{1}{\gamma}} \exp\left(-\frac{N_0^2}{g}(z-z_a)\right).$$

Figure 5 shows the history of the maximum norm of the vertical velocity on a 64×32 (left) and on a 128×64 (right) cell grid. For $N_0 = 0.01$ and $\Delta N = 0.005$ s^{-1}, the maximal vertical velocities are comparable with those obtained with N constant and equal to 0.02 s^{-1}. For the case $N_0 = 0.01$ $\Delta N = 0.01$ s^{-1}, the maximal values of the vertical velocity are about 40% higher. In both cases, the presence of the layer across the topography does not change the order of magnitude of the vertical velocities. These are about 20 times smaller than those obtained, for the same test problem and for the same model equations, with the dynamical core of [9] (results from computations which are not shown). This dynamical core is based on the standard technique of computing the deviations of the pressure from a time independent horizontally constant "reference" hydrostatic profile. Notice also that the results shown in figure 5 could be significantly improved by replacing $\Theta_i^{(0)} = \theta(\varphi(Q_{c_i}), \rho_{c_i})$ with a more accurate approximation to θ. Preliminary results for smooth N show that local linear approximations of θ allow to reduce the vertical velocity error by about two orders of magnitude.

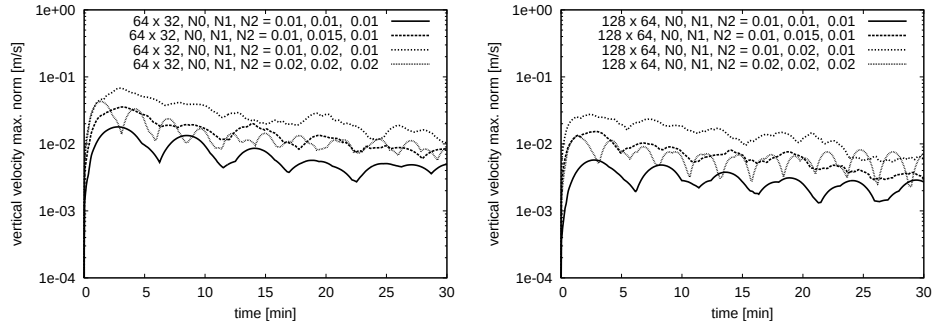

FIG. 5. Hydrostatic flow with piecewise constant buoyancy frequency N at rest above steep topography. Vertical velocity maximum norm (ms^{-1}) versus time (minutes) for $N = N_0 + \Delta N$ for $z_b < z \leq z_a$ and $N = N_0$ otherwise. z_b and z_a are equal to 750 and 1250 m, respectively. Top topography at $z = 2000$ m, see figure 3. Four curves for $(N_0, \Delta N)$ equal to $(0.01, 0)$, $(0.01, 0.005)$, $(0.01, 0.01)$ and $(0.02, 0)$ s^{-1}. 64×32 (left) and 128×64 cells grid.

4.3. Accuracy and robustness

We have mentioned, in the introduction, that standard discretizations of (1) are, for nearly hydrostatic motions, either too inaccurate or too expensive. Another serious drawback is that standard approximations are not robust: numerical solutions are found to be very dependent on details of the algorithm, e.g., on the choice of the limiting function $\mathcal{L}$ and on the algorithm used to recover Q on cells near boundaries.

This sensitivity does not decrease for increasing simulation times and seriously restricts the usability of standard discretizations for, e.g., climate research. It also forces expensive and systematic investigations to assess the effects of small perturbations on the final results. Here we investigate accuracy and robustness of the well balanced method and compare them with those of a standard finite volume approximation. We consider an ideal one-dimensional atmosphere at rest between two flat plates at zero and 18620 m. Pressure, temperature, and density are

$$p(z) = p_0 \exp\left(-\frac{T_0}{\beta}\left(1 - \sqrt{1 - \frac{2\beta g z}{R T_0^2}}\right)\right)\left(1 + \eta \exp\left(-\alpha\left(\frac{z - z_c}{H}\right)^2\right)\right)$$

$$T(z) = T_0\sqrt{1 - \frac{2\beta g z}{R T_0^2}}\,, \qquad \rho(z) = \frac{p(z)}{R T(z)}$$

p_0, T_0, g and R are as in 4.1. β represents the rate of change of temperature with the logarithm of the unperturbed pressure, i.e., for η equal to zero, see [9] and [10]. For this case the atmosphere is in hydrostatic balance. We consider zero velocity initial data with a pressure perturbation defined by $\beta = 42$, $\eta = 10^{-3}$, $\alpha = 60$, $z_c = 9310$ m and $H = 18620$ m. This perturbation generates weak acoustic waves which travel upwards and downwards, are reflected at the solid boundaries, and bounce back and forth between the two

plates. As is known from the theory of weakly nonlinear acoustics, [18], these waves will steepen into weak shocks and begin to dissipate on time scales of order $O(H/Mc)$, equivalent to $O(1/M)$ oscillation cycles. Here c is a characteristic speed of sound and M is the characteristic Mach number for the oscillatory vertical motions. Numerical methods for non-hydrostatic models have to 1) guarantee that these waves generate spurious dynamics neither over short nor over long time scales, and to 2) avoid the CFL time step restrictions associated with the propagation of such waves. In operational methods the second requirement can be met by implicit, semi-implicit, semi-Lagrangian methods, sub-cycling for fast modes, or combinations of such techniques. Here we concentrate on the first issue. Consider the evolution of the initial perturbation at short times. The relative pressure perturbation

$$\frac{\varphi(q(t,\cdot)) - p|_{\eta=0}}{p|_{\eta=0}}$$

at time zero and after 12 sec is shown on the left of figure 6. On the right of the same figure you can see the corresponding velocities (in ms^{-1}). Four curves are plotted in both figures for each time. They correspond to the numerical solutions obtained with a standard method and with the well balanced method presented above. For each method 2 computations are shown: one with the monotonized central limiter and one with no limiter and central slopes, i.e., $\mathcal{L}(a,b) = (a+b)/2$. The curves are not distinguishable because all computations have been done on a very fine grid of 8192 cells. This shows that, as the grid parameter tends to zero, the numerical solution obtained with the well balanced method converges towards the numerical solution obtained with the standard method.

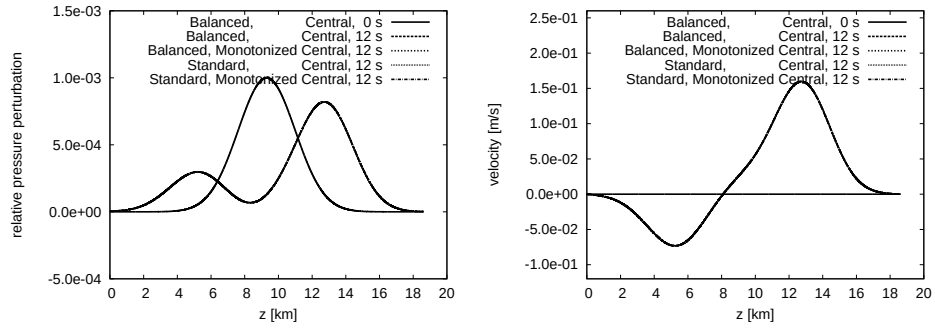

FIG. 6. Hydrostatic flow between flat plates with pressure perturbation. Relative pressure perturbation (left) and velocity (right, ms^{-1}) versus altitude (km) at $t = 0$ and $t = 12$ (sec). Standard and well balanced methods with monotonized central limiter and unlimited central slopes yield indistinguishable results on a high resolution grid of 8192 cells (used as reference solutions below).

When reconstructing a piecewise linear Q from a given set of cell averages, "left" and "right" one-sided approximations to the first derivative of the exact solution have to be evaluated in each cell. These approximations are then

injected into the limiting function $\mathcal{L}$. On a one-dimensional regular grid, left and right approximations can be simply evaluated by computing first order finite differences between the local cell average and the cell averages to the left and to the right. In the first and in the last cell of the grid, however, the left and the right neighbors are missing. As a consequence, the left slope in the first and the right slope in the last cell must be approximated in a different fashion. This can be done in various ways which may depend on the boundary condition imposed on the corresponding boundary. The associated procedures will be called boundary recovery algorithms below.

In the case of a rigid wall boundary condition, one can think of extrapolating the slopes from the inside by means, e.g., of the last one, two, or three inner slopes. Another strategy is to use some prescribed outer state and the values in the first (last) cell to evaluate the left (right) slope.

Figure 7 and 8 show the reference solution of figure 6 and the results obtained, on coarse 32 cell grids, with a standard and with the well balanced method for different boundary recovery algorithms – among others with the algorithm used for computing the reference solution –. Besides being quite inaccurate, the numerical solutions obtained with the standard method on the 32 cell grid depend sensitively on the boundary recovery algorithm. Notice that, for the boundary condition considered here and in absence of a specific stability analysis, there is no apriori argument for choosing a particular algorithm. A stability analysis would help restricting the set of meaningful boundary recovery algorithms but still leave a range of possible choices.

What one really would like to have is a method that does not depend in a critical way on this choice. Figure 8 shows that the well balanced method satisfies this requirement and is far more accurate than the standard method. In fact, the standard method requires about three times more cells to achieve the same accuracy for this test case as the well balanced method.

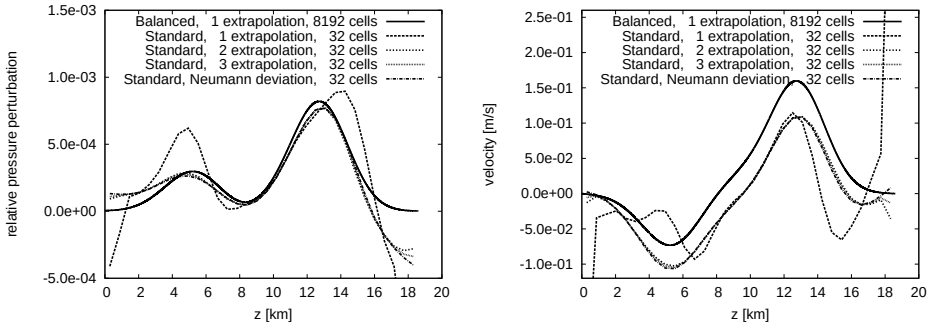

FIG. 7. Hydrostatic flow between flat plates with pressure perturbation. Relative pressure perturbation (left) and velocity (right, ms^{-1}) versus altitude (km) at $t = 12$ (sec). Standard method with unlimited central slopes and 4 different boundary recovery algorithms. Reference solution and 32 grid cells solutions.

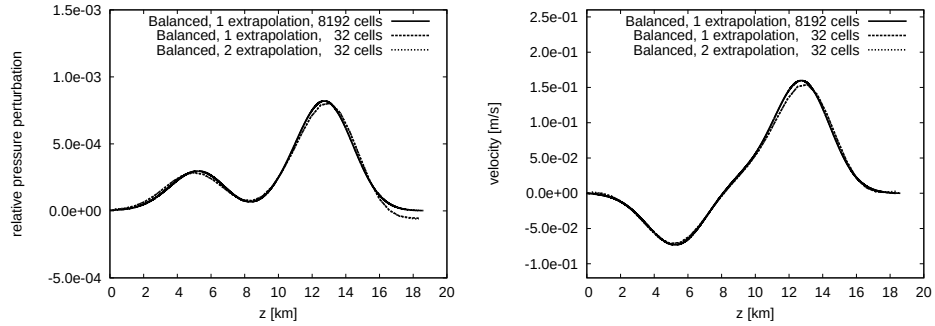

FIG. 8. Hydrostatic flow between flat plates with pressure perturbation. Relative pressure perturbation (left) and velocity (right, ms^{-1}) versus altitude (km) at $t = 12$ (sec). Well balanced method with unlimited central slopes and 2 different boundary recovery algorithms. Reference solution and 32 grid cells solutions.

Figures 9 and 10 show a comparison between standard and well balanced methods for different limiting functions but with a fixed boundary recovery algorithm. We have tested unlimited central slopes, the monotonized central limiter, Van Leer's limiter and the "minmod" limiter, see [42], [45]. For the standard method we have used the boundary recovery algorithm that gave the "best" results in the previous experiment. This corresponds to the dash-dot line in figure 7 and consists of setting to zero the slope of the deviation between the actual state and the initial condition. For the well balanced method we have simply extrapolated the approximate slope (of $q - q^{(0)}$) from the inside.

As expected, the numerical solution obtained with the standard method depends critically on the choice of the limiting function. The same arguments used in the analysis of the sensitivity of the numerical results with respect to perturbations of the boundary recovery algorithm hold here. On very smooth functions – the ones considered here – there is no particular reason to prefer the monotonized central limiter to the Van Leer limiter and "good" numerical methods should not critically depend on this choice.

The numerical results obtained with the well balanced method have this kind of robustness. There is, of course, a significant accuracy gap between unlimited and limited computations. This is a well known problem which stems from the fact that, even on smooth solutions, the accuracy of the limited scheme in the vicinity of local extrema is not better than first order. This problem affects both the standard and the well balanced method. Note, however, that the effects of local accuracy losses on the standard method are devastating. Also notice that the balancing approach proposed here can be applied to more sophisticated recovery algorithms designed to avoid local accuracy losses, see [17] and references therein.

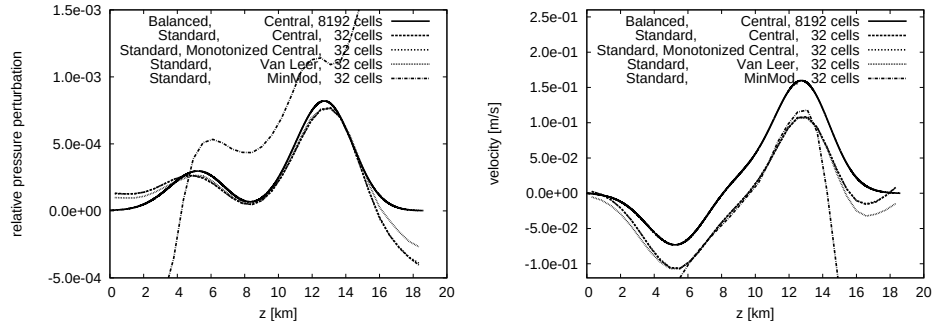

FIG. 9. Hydrostatic flow between flat plates with pressure perturbation. Relative pressure perturbation (left) and velocity (right, ms^{-1}) versus altitude (km) at $t = 12$ (sec). Standard method with unlimited central slopes and monotonized central, Van Leer and minmod limiters. Reference solution and 32 grid cells solutions.

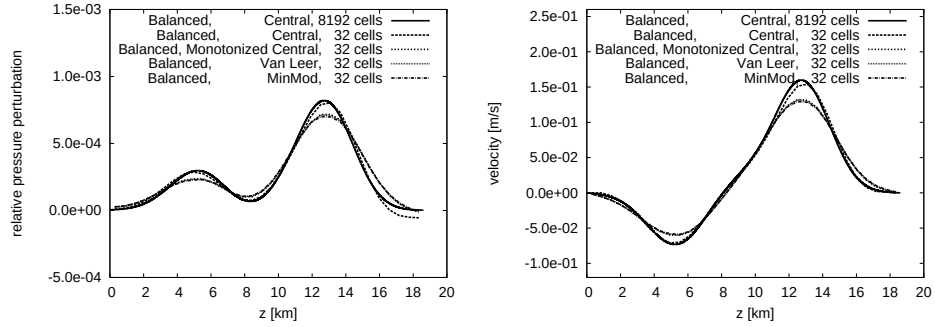

FIG. 10. Hydrostatic flow between flat plates with pressure perturbation. Relative pressure perturbation (left) and velocity (right, ms^{-1}) versus altitude (km) at $t = 12$ (sec). Well balanced method with unlimited central slopes and monotonized central, Van Leer and minmod limiters. Reference solution and 32 grid cells solutions.

4.4. Convergence rate study

In this experiment we investigate the behavior of the well balanced method when the grid parameter tends to zero. We consider a dry flow past the idealized topography

$$z_{\mathrm{b}}(x) = h \exp\left(-\frac{x^2}{a^2}\right) \cos^2\left(\frac{\pi x}{\lambda}\right) \qquad \forall x \in I\!R$$

with $h = 250$ m, $a = 5$ km and $\lambda = 4$ km. In the initial condition the buoyancy frequency (19) is constant and equal to 0.01 s^{-1}. p_0 and T_0 are equal to 10^5 Nm^{-2} and 273.16 °K, respectively. The vertical profiles of pressure, density and temperature are

$$p(z) = p_0 \left(1 - \frac{\gamma - 1}{\gamma} \frac{1}{RT_0} \frac{g^2}{N^2} \left(1 - \exp -\frac{N^2}{g} z\right)\right)^{\frac{\gamma}{\gamma - 1}}$$

$$\rho(z) = \rho_0 \left(\frac{p(z)}{p_0}\right)^{\frac{1}{\gamma}} \exp -\frac{N^2}{g} z\,, \qquad T(z) = \frac{p(z)}{R\rho(z)}$$

TABLE 1
2-norm errors and convergence rates after about 17 minutes of simulation time.

	density	rate	hor. vel.	rate	ver. vel	rate	pressure	rate
400×64	4.341		1.310		1.468		3.531	
800×128	1.369	1.66	0.719	0.87	0.433	1.75	0.888	1.99
1600×256	0.361	1.92	0.029	1.32	0.014	1.59	0.222	2.00

for z between zero and 19500 m. The computational domain is 200 km wide. The horizontal velocity is equal to 10 ms^{-1} between zero and 10395 m and decreases linearly to zero between 10395 m and 19500 m. The vertical velocity is zero in the whole domain. This test problem has been proposed in [41] to investigate the impact of a new terrain-following grid on the Canadian MC2 model [2].

The basic grid consists of 400×64 cells. All cells have a width of 500 m. The vertical cell size is about 300 m. Beside the basic grid, we consider refinements of 800×128, 1600×256 and 3200×512 cells. Table 1 shows the errors and the convergence rates of the well balanced method at short times in the 2-norm. The results are consistent with second order accuracy.

Figure 11 shows the steady state results obtained with the basic grid – 8 cells per half wavelength i.e. $\lambda = 8\Delta x$ – and with grids of 10, 12 and 16 cells per half wavelength (500×80, 600×96 and 800×128 cells grid, respectively). On the coarsest grid the topography is hardly resolved and the numerical solution has an unphysical wave pattern. This is in agreement with the results discussed in [41]. As the grid is refined, the unphysical pattern disappears and the numerical solution is in good agreement with the linear analytical solution. Notice that, here, we are using the standard, unsmoothed "sigma" coordinate, see [41] page 16 and figure 13.

In a recent work with an early version of the Weather Research and Forecast model (WRF) prototype, see [24], Klemp et. al. show that, on a fixed grid and for a given choice of a background state, numerical approximations of different order of accuracy along different coordinate surfaces – called "inconsistent" approximations in [24] – can lead to unphysical wave patterns like those observed in figure 11 on rough grids. In other words, the scheme can be sensitive w.r.t. perturbation of the discrete differential operators: slightly different second order accurate approximations lead, on a fixed grid and for a given choice of the background state, to qualitatively different numerical results.

These results are disturbing and the authors propose a detailed analysis of the linear steady Boussinesq equations to explain them. This analysis show that "inconsistent" approximations can lead to inhomogeneous terms in the

wave equation for the approximate vertical velocity amplitude. Provided the terrain topography has significant amplitudes at wave numbers in the vicinity of the Scorer parameter, these inhomogeneous terms lead to singularities in the integrand of the equation for the vertical velocity.

Here we are using piecewise linear reconstruction and slopes are computed by means of second order central finite differences along both coordinate lines, see algorithm 1. Thus, our numerical results suggest that the unphysical flow pattern observed in in [24] may appear, on coarse grids and for this particular test case, no matter whether approximations are "inconsistent" or not.

Having in mind the robustness problem identified in [24], it is interesting to investigate, how sensitive our methods is w.r.t. perturbations of the recovery algorithm in general and of the local hydrostatic balanced state in particular. Figure 12 shows the steady state results obtained, for the same problem and on the same grids of figure 11, with a slightly different recovery algorithm. Here we have replaced the piecewise constant entropy profiles of step 2 of algorithms 1 and 2 by means of piecewise linear approximations:

$$P_{i,j}^{(0)}/{R_{i,j}^{(0)}}^{\gamma} = \varphi(Q_{c_{i,j}})/R_{c_{i,j}}^{\gamma} + \nabla_{c_{i,j}}\Theta\cdot(\boldsymbol{x}-\boldsymbol{x}_{i,j})$$

In the above equation the discrete entropy gradient $\nabla_{c_{i,j}}\Theta$ has been computed by standard second order central finite differences along the grid lines. Moreover, we have replaced the left and right approximations to the gradient of $q-q^{(0)}$ in step 6 of algorithm 1 with the simpler (but still "consistent" and second order accurate) approximations:

$$\begin{aligned} G\delta Q_{i\pm,j}^{k} &:= \delta Q_{i\pm1,j}\frac{\partial y^1}{\partial x^k} + \frac{1}{2}\left(\delta Q_{i,j+1} - \delta Q_{i,j-1}\right)\frac{\partial y^2}{\partial x^k} \\ G\delta Q_{i,j\pm}^{k} &:= \frac{1}{2}\left(\delta Q_{i+1,j} - \delta Q_{i-1,j}\right)\frac{\partial y^1}{\partial x^k} + \delta Q_{i,j\pm1}\frac{\partial y^2}{\partial x^k} \end{aligned} \tag{20}$$

These results are better than the ones shown in figure 11 in the sense that the erroneous flow pattern disappears for resolutions somewhere between $\lambda = 8\Delta x$ and $\lambda = 10\Delta x$ (between $\lambda = 12\Delta x$ and $\lambda = 16\Delta x$ in figure 11). They are consistent with the results discussed in section 4.3 and show that the balancing approach proposed here lead to robust numerical methods: slightly different second order approximations and slightly different reconstructions of the local balanced state lead to slightly different numerical results. This is confirmed by numerical experiments with local piecewise linear entropy profiles but left and right approximations to the gradient of $q-q^{(0)}$ as in step 6 of algorithm 1. These results (not shown here) are somewhere between those of figure 11 and those shown in figure 12.

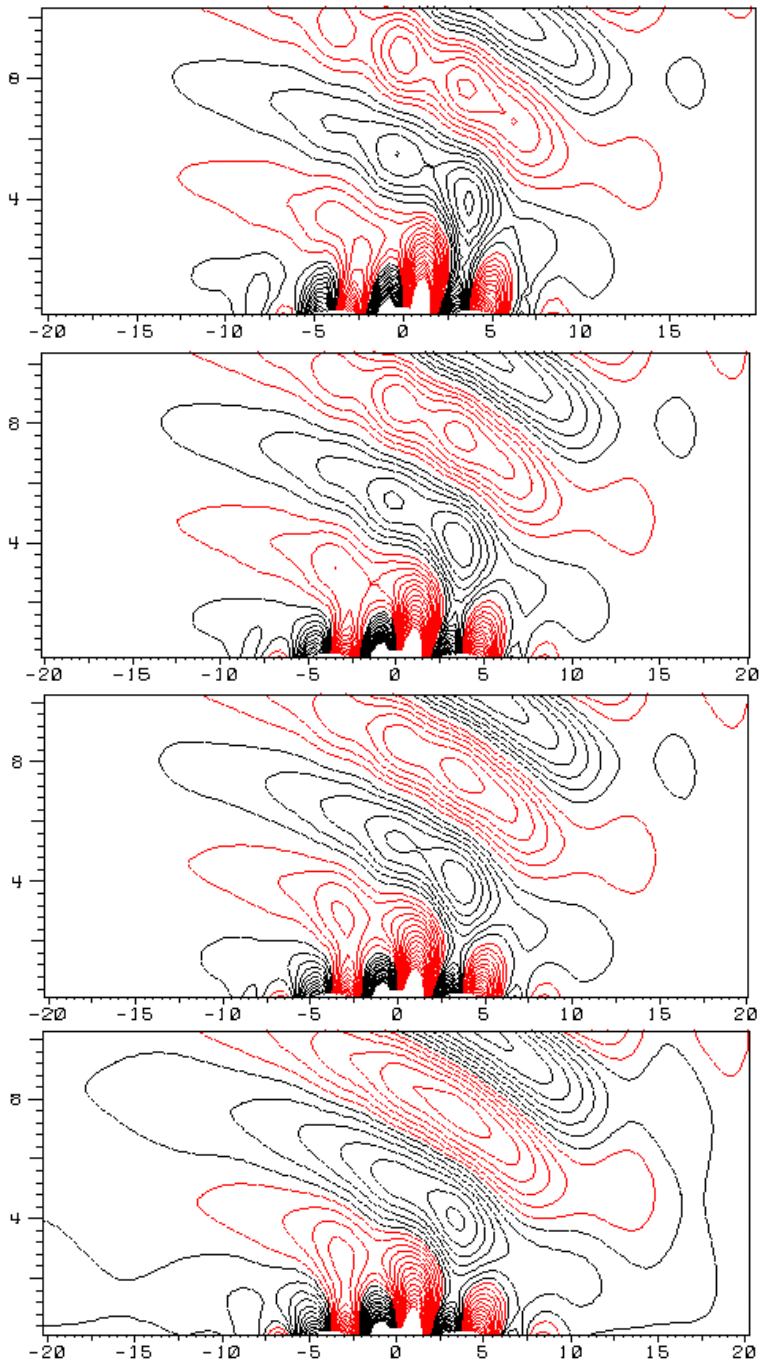

FIG. 11. Linear non-hydrostatic flow. Steady state vertical velocity near topography (40×10.8 km sub-domain). 30 contour lines between -1 and -0.05 and between 0.05 and 1 ms^{-1}. Contour interval 0.05 ms^{-1}. From top to bottom: 8, 10, 12 and 16 cells per half wavelength.

4.5. Linear, non-hydrostatic gravity waves

In the last experiment we investigate the behavior of the well balanced method for a linear non-hydrostatic flow above a mountain-like obstacle.

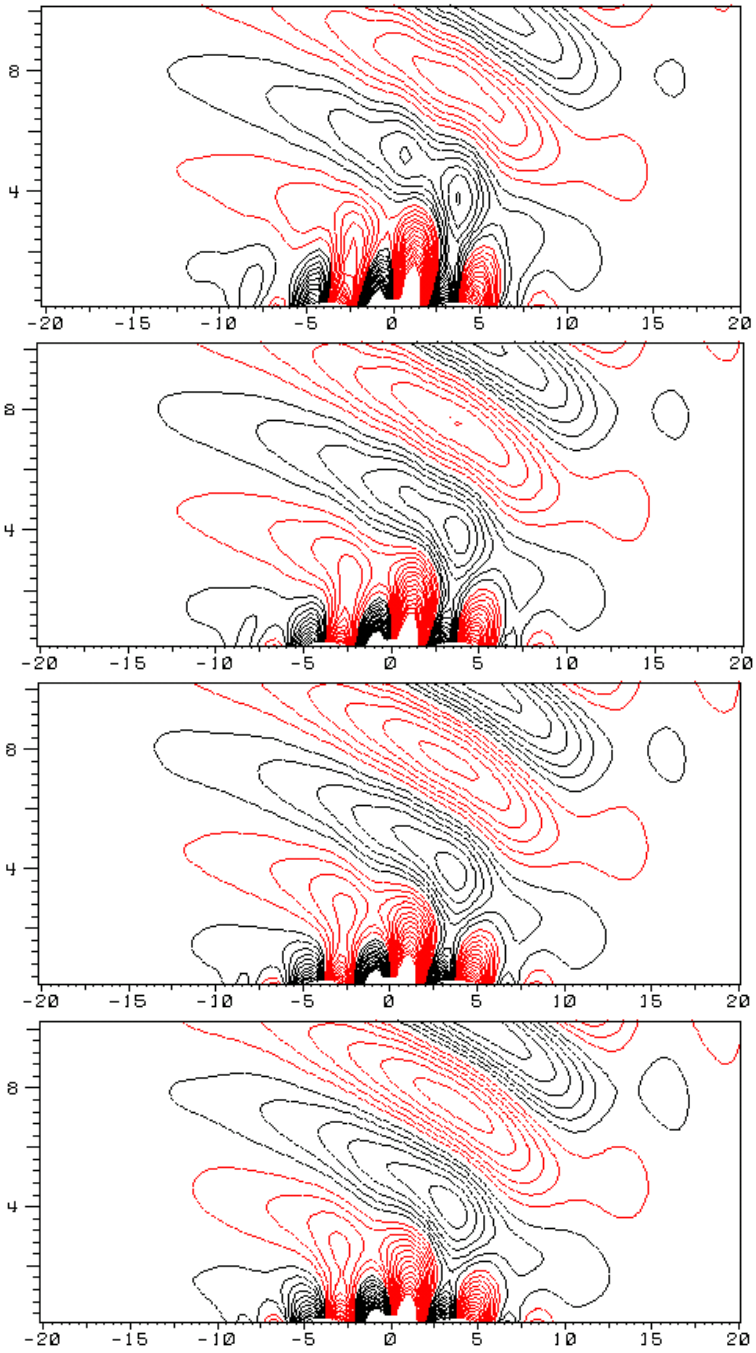

FIG. 12. Linear non-hydrostatic flow. Steady state vertical velocity near topography (40×10.8 km sub-domain). Reconstruction of the local balanced state via piecewise linear entropy distribution and left and right local approximations to the gradient of $q - q^{(0)}$ as in 20. 30 contour lines between -1 and -0.05 and between 0.05 and 1 ms^{-1}. Contour interval 0.05 ms^{-1}. From top to bottom: 8, 10, 12 and 16 cells per half wavelength.

Here linear means that the Froude number based on the buoyancy frequency of the initial data and on the mountain height h, $u/(Nh)$, is much larger than one. Non-hydrostatic means, in this context, that the Froude number based on the horizontal size of the obstacle a, $u/(Na)$ is about unity. This is a standard test problem for numerical methods for weather prediction. In the limit for $u/(Nh) \to \infty$ steady state analytical solutions have been computed in [37], [32], [44], [8].

The initial conditions consist of an isothermal atmosphere with p_0, T_0 equal to 10^5 Nm^{-2} and 273.16 °K, respectively. The acceleration of gravity g and the gas constants R and γ are, as in the previous examples, equal to 10 ms^{-2}, 287 NmKg^{-1}°K^{-1} and 1.4, respectively. In such atmosphere the buoyancy frequency N is constant and about 0.0191 s^{-1}. This gives, with an initial horizontal velocity of 19.1 ms^{-1} and h, a equal to 100 and 1000 m, values of $u/(Nh)$ and $u/(Na)$ of 10 and 1, respectively.

As in the first and in the second experiment, the topography $z_{\rm b}$ is a smooth function

$$z_{\rm b}(x) = \frac{h}{\left(1 + \left(\frac{x}{a}\right)^2\right)^{3/2}} \qquad \forall x \in I\!R$$

of the horizontal space coordinate x. Computational domain and finite volumes grid are shown on the left of figure 13. On the right you can see the isolines of the vertical velocity. The results are in good qualitative agreement with those reported in the literature and with the linear solution. Notice that, in this test problem, the quality of the numerical results very much depends on the capability to avoid spurious reflection of the gravity waves at the lateral boundaries and at the top of the atmosphere. The problem of constructing non-reflective (radiation, transparent) boundary conditions for modeling open artificial boundaries for the compressible Euler equation is still open, see [11], [15] for a review of some popular approaches.

In most production codes this problem is partially circumvented by introducing ad hoc "sponge" layers near the artificial boundaries. In these layers the equations of motion are modified by means of correction terms which drive the numerical solution towards some prescribed state. Here we have followed a different approach. At the lateral boundaries we have used boundary conditions based on the theory of characteristics. At the top of the atmosphere we have prescribed an external fixed state. This state is used, together with another one recovered from the inside, to compute the fluxes through the boundary. The (approximate) Riemann problems associated with the computation of the numerical flux, however, have not been defined in the direction normal to the boundary. Instead we have used a rough estimate of the gradient of the solution in the vicinity of the upper boundary to define a time dependent direction. This direction has been used to solve the approximate Riemann problems on the boundary.

This approach requires further investigation and the results presented in figure 13 are preliminary. An investigation of the new approach will be presented in a separate work.

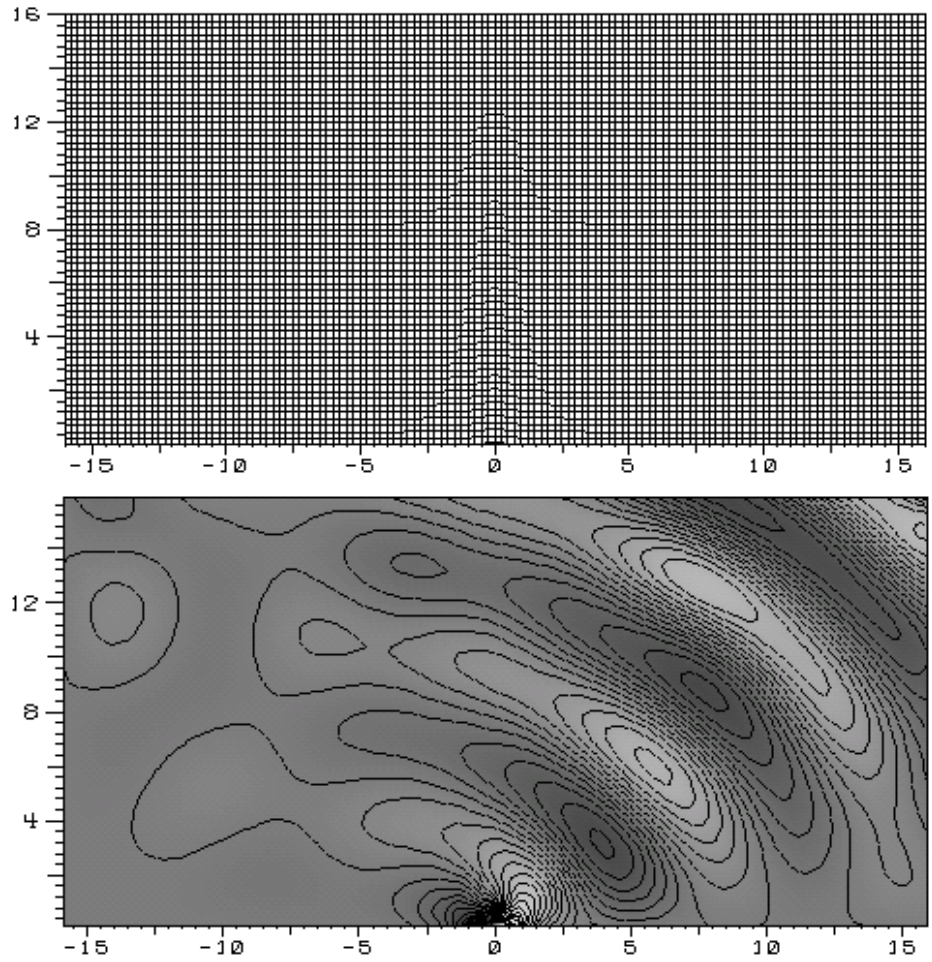

FIG. 13. Linear non-hydrostatic flow. Top: computational domain (km) and finite volumes grid (128×64 cells). Bottom: vertical velocity (ms^{-1}).

5. CONCLUSIONS

We have shown that standard finite volume Godunov-type schemes for compressible flows can be modified to provide accurate solutions for a large class of nearly hydrostatic flows on terrain-following curvilinear grids. These flows are relevant in numerical weather prediction and regional climate simulations and the balancing approach presented here can be easily applied to other kinds of grids, e.g. unstructured grids and, obviously, Cartesian grids.

Our investigations indicate that the standard discretization of the pressure gradient and of the gravitational source term is responsible for failures to accurately describe nearly hydrostatic motions. This statement holds for any choice of coordinates in which the governing equations are formulated, and our balancing strategy should be general enough to be used in conjunction with any coordinate system.

Balancing approaches based on the formulation of the governing equations in terms of deviations from a prescribed, constant in time hydrostatic background state, often fail to describe stationary hydrostatic states at rest over topography on terrain-following curvilinear grids. The same approaches usually succeed on Cartesian grids over flat topography when the numerical solution and the hydrostatic background state coincide. For finite deviations from the prescribed background state, however, standard methods will generally fail both on curvilinear and on Cartesian grids.

Grid skewness has, of course, a detrimental effect on the accuracy of discretizations and leads to spurious entropy generation [1] and unphysical mountain drag. As pointed out in [41], some of these effects can be alleviated by designing suitably smoothed curvilinear grids.

Of course, both standard methods and well balanced methods take advantage of more regular grids. For standard applications in numerical weather forecasting and climate simulation, where the topography on a fixed grid is hardly resolved, the introduction of smoothed topography and/or orthogonal terrain following grids may significantly improve the quality of the numerical results, see [5].

The well balanced method presented here achieves balancing while avoiding the computation of global approximations of a time-dependent hydrostatic background state. Instead, this state is approximated locally in the recovery stage of a standard MUSCL [25], [26], [27], [28], [29] approach. This requires the solution of a small number of scalar ordinary differential equations for each grid cell per flux evaluation. In most cases these solutions can be computed analytically. Thus, the well balanced method requires very little extra computational costs. This allows one to significantly reduce the number of grid cells needed to approximate nearly hydrostatic motions with acceptable accuracy.

The new method is robust against details of the implementation, e.g., the choice of slope limiting functions, or the particulars of boundary condition discretizations, and second order accurate in space and in time. It inherits the conservation properties of the underlying Godunov-type scheme: mass and total energy are conserved exactly, independently of the grid size. These properties – robustness, accuracy and conservation – seem to be essential for coarse grid, long time simulations such as those typical of regional climate modeling.

Non-hydrostatic models for numerical weather forecasting could also take advantage of the balancing approach proposed here to 1) increase the accuracy in the vicinity of the hydrostatic regime and 2) improve the model robustness against implementation details and grid geometry.

ACKNOWLEDGMENT

The authors thank the reviewers, whose comments have triggered various nontrivial improvements of the paper. This research was funded partly by the Deutsche Forschungsgemeinschaft, grant DFG KL 611/6-3. This work heavily relies on free software, among others on the CGG compiler, Emacs, LaTeX, gnuplot, MeshTV, on the Debian / GNU Linux operating system and on the `util` library of D. Hempel and O. Friedrich. It is our pleasure to thank all developers of these excellent products.

REFERENCES

1. J. G. Andrews. Spurious entropy generation as a mesh quality indicator. Oxford University Computing Laboratory, Numerical Analysis Group, Report Number 93/12, 1993.
2. R. Benoit, M. Desdagné, P. Pellerin, Y. Chartier, and S. Desjardins. The Canadian MC2: A semi-Lagrange, semi-implicit wide-band atmospheric model suited for fine-scale process studies and simulation. *Month. Wea. Rev.*, 125:2382–2415, 1997.
3. L. Bonaventura. A Semi-implicit Semi-Lagrangian Scheme Using the Height Coordinate for a Nonhydrostatic and Fully Elastic Model of Atmospheric Flows. *J. Compu. Phys.*, 158:186–213, 2000.
4. N. Botta, R. Klein, and A. Almgren. Asymptotic analysis of a dry atmosphere. In P. Neittaanmäki, T. Tiihonen, and P. Tarvainen, editors, *Proceedings of the 3rd European Conference ENUMATH 99: Numerical Mathematics and Advanced Applications*. World Scientific, Singapore, New Jersey, London, Hong Kong, 2000.
5. N. Botta, R. Klein, and S. Puetz. Conservative methods for non-hydrostatic models: Construction and validation. Lecture presented at Fourth International SRNWP Workshop on Non-Hydrostatic Modelling in Bad Orb, 24 - 26 September 2001, available at http://www.pik-potsdam.de/ botta/interests/interests.html, 2001.
6. P. Cargo and A. Y. Le Roux. Un schéma équilibre adapté au modèle d'atmosphère avec termes de gravité. *C. R. Acad. Sci. Paris*, 318 Série I:73–76, 1994.
7. Corby, A. Gilchrist, and Newson R. L. A general circulation model of the atmosphere suitable for long period integration. *QJRMS*, 98:809–832, 1972.
8. R. Rotunno D. J. Muraki. Revisiting Queney's Flow over Mesoscale Topography. Technical report, AMS mountain meteorology meeting, 2000.
9. G. Doms and U. Schättler. The nonhydrostatic limited-area model lm (lokal-modell) of dwd: Part i, scientific documentation. Deutscher Wetterdienst, 1997.
10. J. Dudhia. A nonhydrostatic version of the Penn State / NCAR mesoscale model: Validation tests and simulation of an Atlantic cyclone and cold front. *Mon. Wea. Rev.*, 121:1493–1513, 1993.
11. D. R. Durran. *Numerical Methods for Wave Equations in Geophysical Fluid Dynamics*. Springer, 1999.
12. B. Einfeldt. Zur Numerik der stoßauflösenden Verfahren. Dissertation, RWTH Aachen, 1988.
13. T. Gal-Chen and R. C. J. Sommerville. Numerical solutions of the Navier-Stokes equations with topography. *J. Comput. Phys.*, 17:276–310, 1975.
14. A. E. Gill. *Atmosphere-Ocean Dynamics*. Academic Press, 1982.
15. D. Givoli. Non-reflecting boundary conditions. *J. Comput. Phys.*, 94:1–29, 1991.
16. J. M. Greenberg and A. Y. Le Roux. A well-balanced scheme for the numerical processing of source terms in hyperbolic equations. *SIAM Numer. Anal.*, 33(1):1–16, 1996.
17. D. Hempel. *Rekunstruktionsverfahren auf unstrukturierten Gittern zur numerischen Simulation von Erhaltungsprinzipien*. PhD thesis, Universität Hamburg, Fachbereich Mathematik, 1999.
18. J. Hunter and J. Keller. Weakly nonlinear high frequency waves. *Commun. Pure Appl. Math.*, 36:547–569, 1983.
19. P. Jenny and B. Müller. Rankine-Hugoniot-Riemann Solver Considering Source Terms and Multidimensional Effects. *J. Comp. Phys.*, 145:575–610, 1998.

20. W. A. Gallus Jr. and J. B. Klemp. Behavior of Flow over Step Orography. *Month. Wea. Rev.*, 128:1153–1164, 2000.

21. H. Kapitza and D. P. Eppel. The Nonhydrostatic Mesoscale Model GESIMA. part I: Dynamical Equations and Tests. *Beitr. Phys. Atmosph.*, 65(2):129–146, 1992.

22. R. Klein. Semi-implicit extension of a godunov-type scheme based on low mach number asymptotics i: One-dimensional flow. *Journ. of Comp. Physics*, 121:213–237, 1995.

23. R. Klein. Asymptotic analyses for atmospheric flows and the construction of asymptotically adaptive numerical methods. *ZAMM - Z. Angew. Math. Mech.*, 80:765–777, 2000.

24. J. B. Klemp, W. C. Skamarock, and O. Fuhrer. Numerical consistency of metric terms in terrain-following coordinates. *to be submitted for publication to Month. Wea. Rev.*

25. B. van Leer. Towards the ultimate conservative difference scheme. I. The quest of monotonicity. *Lecture Notes in Phys.*, 18:163–168, 1973.

26. B. van Leer. Towards the ultimate conservative difference scheme. II. Monotonicity and conservation combined in a second-order scheme. *J. Comput. Phys.*, 14:361–370, 1974.

27. B. van Leer. Towards the ultimate conservative difference scheme. III. Upstream-centered finite-difference schemes for ideal compressible flow. *J. Comput. Phys.*, 23:263–275, 1977.

28. B. van Leer. Towards the ultimate conservative difference scheme. IV. A new approach to numerical convection. *J. Comput. Phys.*, 23:276–299, 1977.

29. B. van Leer. Towards the ultimate conservative difference scheme. V. A second-order sequel to Godunov's method. *J. Comp. Phys.*, 32:101–136, 1979.

30. R. J. LeVeque. *Numerical Methods for Conservation Laws*. Birkhäuser, Basel, 1990.

31. R. J. LeVeque. Balancing source terms and flux gradients in high-resolution Godunov methods. *J. Comput. Phys.*, 146:346–365, 1998.

32. Ed. M. A. Alaka. The airflow over mountains. Technical report, WMO Tech. Note 34, 1960.

33. A.J. Majda and R. Klein. Systematic multi-scale models for the tropics. *J. Atmos. Sci.*, 2002. to be submitted.

34. Nakamura. Dynamical effects of mountains on the general circulation of the atmosphere. I. development of finite-difference schemes suitable for incorporating mountains. *J. Meteor. Soc. Japan*, 56:317–339, 1978.

35. J. Pedlosky. *Geophisical fluid dynamics*. Springer, 2nd edition, 1987.

36. J.-P. Pinty, R. Benoit, E. Richard, and R. Laprise. Simple Tests of a Semi-Implicit Semi-Lagrangian Model on 2D Mountain Wave Problems. *Month. Wea. Rev.*, 123:3042–3057, 1995.

37. P. Queney. The problem of air flow over mountains: A summary of theoretical studies. *Bull. Amer. Meteor. Soc.*, 29:16–26, 1948.

38. Courant R., Friedrichs K. O., and Lewy H. Über die partiellen Differenzengleichungen der Physik. *Math. Ann.*, 100:32, 1928.

39. Klainerman S. and Majda A. J. Compressible and incompressible fluids. *Commun. Pure Appl. Math.*, 35:629, 1982.

40. K. Saito, G. Doms, U. Schaettler, and J. Steppeler. 3-D Mountain Waves by the Lokal-Modell of DWD and the MRI Mesoscale Nonhydrostatic Model. *Papers in Meteorology and Geophysics*, 49(1):7–19, 1998.

41. C. Schär, D. Leuenberger, O. Fuhrer, D. Lüthi, and C. Girard. A new terrain-following vertical coordinate formulation for atmospheric prediction models. *submitted for publication to Month. Wea. Rev.*

42. C.W. Schulz-Rinne. *The Riemann problem for two-dimensional gas dynamics and new limiters for high-order schemes*. PhD thesis, Swiss Federal Institute of Technology, Diss. ETH No. 10297, 1993.

43. Simmons and D. M. Burridge. An energy and angular-momentum conserving vertical finite-difference scheme and hybrid vertical coordinates. *Mon. Wea. Rev.*, 109:758–766, 1981.

44. R. B. Smith. Linear theory of stratified hydrostatic flow past an isolated mountain. *Tellus*, 32:348–364, 1980.

45. P. K. Sweby. High resolution schemes using flux limiters for hyperbolic conservation laws. *SIAM J. Numer. Anal.*, 21:995–1011, 1984.

PIK Report-Reference:

No. 1 3. Deutsche Klimatagung, Potsdam 11.-14. April 1994
Tagungsband der Vorträge und Poster (April 1994)

No. 2 Extremer Nordsommer '92
Meteorologische Ausprägung, Wirkungen auf naturnahe und vom Menschen beeinflußte Ökosysteme, gesellschaftliche Perzeption und situationsbezogene politisch-administrative bzw. individuelle Maßnahmen (Vol. 1 - Vol. 4)
H.-J. Schellnhuber, W. Enke, M. Flechsig (Mai 1994)

No. 3 Using Plant Functional Types in a Global Vegetation Model
W. Cramer (September 1994)

No. 4 Interannual variability of Central European climate parameters and their relation to the large-scale circulation
P. C. Werner (Oktober 1994)

No. 5 Coupling Global Models of Vegetation Structure and Ecosystem Processes - An Example from Arctic and Boreal Ecosystems
M. Plöchl, W. Cramer (Oktober 1994)

No. 6 The use of a European forest model in North America: A study of ecosystem response to climate gradients
H. Bugmann, A. Solomon (Mai 1995)

No. 7 A comparison of forest gap models: Model structure and behaviour
H. Bugmann, Y. Xiaodong, M. T. Sykes, Ph. Martin, M. Lindner, P. V. Desanker, S. G. Cumming (Mai 1995)

No. 8 Simulating forest dynamics in complex topography using gridded climatic data
H. Bugmann, A. Fischlin (Mai 1995)

No. 9 Application of two forest succession models at sites in Northeast Germany
P. Lasch, M. Lindner (Juni 1995)

No. 10 Application of a forest succession model to a continentality gradient through Central Europe
M. Lindner, P. Lasch, W. Cramer (Juni 1995)

No. 11 Possible Impacts of global warming on tundra and boreal forest ecosystems - Comparison of some biogeochemical models
M. Plöchl, W. Cramer (Juni 1995)

No. 12 Wirkung von Klimaveränderungen auf Waldökosysteme
P. Lasch, M. Lindner (August 1995)

No. 13 MOSES - Modellierung und Simulation ökologischer Systeme - Eine Sprachbeschreibung mit Anwendungsbeispielen
V. Wenzel, M. Kücken, M. Flechsig (Dezember 1995)

No. 14 TOYS - Materials to the Brandenburg biosphere model / GAIA
Part 1 - Simple models of the "Climate + Biosphere" system
Yu. Svirezhev (ed.), A. Block, W. v. Bloh, V. Brovkin, A. Ganopolski, V. Petoukhov, V. Razzhevaikin (Januar 1996)

No. 15 Änderung von Hochwassercharakteristiken im Zusammenhang mit Klimaänderungen - Stand der Forschung
A. Bronstert (April 1996)

No. 16 Entwicklung eines Instruments zur Unterstützung der klimapolitischen Entscheidungsfindung
M. Leimbach (Mai 1996)

No. 17 Hochwasser in Deutschland unter Aspekten globaler Veränderungen - Bericht über das DFG-Rundgespräch am 9. Oktober 1995 in Potsdam
A. Bronstert (ed.) (Juni 1996)

No. 18 Integrated modelling of hydrology and water quality in mesoscale watersheds
V. Krysanova, D.-I. Müller-Wohlfeil, A. Becker (Juli 1996)

No. 19 Identification of vulnerable subregions in the Elbe drainage basin under global change impact
V. Krysanova, D.-I. Müller-Wohlfeil, W. Cramer, A. Becker (Juli 1996)

No. 20 Simulation of soil moisture patterns using a topography-based model at different scales
D.-I. Müller-Wohlfeil, W. Lahmer, W. Cramer, V. Krysanova (Juli 1996)

No. 21 International relations and global climate change
D. Sprinz, U. Luterbacher (1st ed. July, 2n ed. December 1996)

No. 22 Modelling the possible impact of climate change on broad-scale vegetation structure - examples from Northern Europe
W. Cramer (August 1996)

No. 23 A methode to estimate the statistical security for cluster separation
F.-W. Gerstengarbe, P.C. Werner (Oktober 1996)

No. 24 Improving the behaviour of forest gap models along drought gradients
H. Bugmann, W. Cramer (Januar 1997)

No. 25 The development of climate scenarios
P.C. Werner, F.-W. Gerstengarbe (Januar 1997)

No. 26 On the Influence of Southern Hemisphere Winds on North Atlantic Deep Water Flow
S. Rahmstorf, M. H. England (Januar 1977)

No. 27 Integrated systems analysis at PIK: A brief epistemology
A. Bronstert, V. Brovkin, M. Krol, M. Lüdeke, G. Petschel-Held, Yu. Svirezhev, V. Wenzel (März 1997)

No. 28 Implementing carbon mitigation measures in the forestry sector - A review
M. Lindner (Mai 1997)

No. 29 Implementation of a Parallel Version of a Regional Climate Model
M. Kücken, U. Schättler (Oktober 1997)

No. 30 Comparing global models of terrestrial net primary productivity (NPP): Overview and key results
W. Cramer, D. W. Kicklighter, A. Bondeau, B. Moore III, G. Churkina, A. Ruimy, A. Schloss, participants of "Potsdam '95" (Oktober 1997)

No. 31 Comparing global models of terrestrial net primary productivity (NPP): Analysis of the seasonal behaviour of NPP, LAI, FPAR along climatic gradients across ecotones
A. Bondeau, J. Kaduk, D. W. Kicklighter, participants of "Potsdam '95" (Oktober 1997)

No. 32 Evaluation of the physiologically-based forest growth model FORSANA
R. Grote, M. Erhard, F. Suckow (November 1997)

No. 33 Modelling the Global Carbon Cycle for the Past and Future Evolution of the Earth System
S. Franck, K. Kossacki, Ch. Bounama (Dezember 1997)

No. 34 Simulation of the global bio-geophysical interactions during the Last Glacial Maximum
C. Kubatzki, M. Claussen (Januar 1998)

No. 35 CLIMBER-2: A climate system model of intermediate complexity. Part I: Model description and performance for present climate
V. Petoukhov, A. Ganopolski, V. Brovkin, M. Claussen, A. Eliseev, C. Kubatzki, S. Rahmstorf (Februar 1998)

No. 36 Geocybernetics: Controlling a rather complex dynamical system under uncertainty
H.-J. Schellnhuber, J. Kropp (Februar 1998)

No. 37 Untersuchung der Auswirkungen erhöhter atmosphärischer CO_2-Konzentrationen auf Weizenbestände des Free-Air Carbondioxid Enrichment (FACE) - Experimentes Maricopa (USA)
Th. Kartschall, S. Grossman, P. Michaelis, F. Wechsung, J. Gräfe, K. Waloszczyk, G. Wechsung, E. Blum, M. Blum (Februar 1998)

No. 38 Die Berücksichtigung natürlicher Störungen in der Vegetationsdynamik verschiedener Klimagebiete
K. Thonicke (Februar 1998)

No. 39 Decadal Variability of the Thermohaline Ocean Circulation
S. Rahmstorf (März 1998)

No. 40 SANA-Project results and PIK contributions
K. Bellmann, M. Erhard, M. Flechsig, R. Grote, F. Suckow (März 1998)

No. 41 Umwelt und Sicherheit: Die Rolle von Umweltschwellenwerten in der empirisch-quantitativen Modellierung
D. F. Sprinz (März 1998)

No. 42 Reversing Course: Germany's Response to the Challenge of Transboundary Air Pollution
D. F. Sprinz, A. Wahl (März 1998)

No. 43 Modellierung des Wasser- und Stofftransportes in großen Einzugsgebieten. Zusammenstellung der Beiträge des Workshops am 15. Dezember 1997 in Potsdam
A. Bronstert, V. Krysanova, A. Schröder, A. Becker, H.-R. Bork (eds.) (April 1998)

No. 44 Capabilities and Limitations of Physically Based Hydrological Modelling on the Hillslope Scale
A. Bronstert (April 1998)

No. 45 Sensitivity Analysis of a Forest Gap Model Concerning Current and Future Climate Variability
P. Lasch, F. Suckow, G. Bürger, M. Lindner (Juli 1998)

No. 46 Wirkung von Klimaveränderungen in mitteleuropäischen Wirtschaftswäldern
M. Lindner (Juli 1998)

No. 47 SPRINT-S: A Parallelization Tool for Experiments with Simulation Models
M. Flechsig (Juli 1998)

No. 48 The Odra/Oder Flood in Summer 1997: Proceedings of the European Expert Meeting in Potsdam, 18 May 1998
A. Bronstert, A. Ghazi, J. Hladny, Z. Kundzewicz, L. Menzel (eds.) (September 1998)

No. 49 Struktur, Aufbau und statistische Programmbibliothek der meteorologischen Datenbank am Potsdam-Institut für Klimafolgenforschung
H. Österle, J. Glauer, M. Denhard (Januar 1999)

No. 50 The complete non-hierarchical cluster analysis
F.-W. Gerstengarbe, P. C. Werner (Januar 1999)

No. 51 Struktur der Amplitudengleichung des Klimas
A. Hauschild (April 1999)

No. 52 Measuring the Effectiveness of International Environmental Regimes
C. Helm, D. F. Sprinz (Mai 1999)

No. 53 Untersuchung der Auswirkungen erhöhter atmosphärischer CO_2-Konzentrationen innerhalb des Free-Air Carbon Dioxide Enrichment-Experimentes: Ableitung allgemeiner Modellösungen
Th. Kartschall, J. Gräfe, P. Michaelis, K. Waloszczyk, S. Grossman-Clarke (Juni 1999)

No. 54 Flächenhafte Modellierung der Evapotranspiration mit TRAIN
L. Menzel (August 1999)

No. 55 Dry atmosphere asymptotics
N. Botta, R. Klein, A. Almgren (September 1999)

No. 56 Wachstum von Kiefern-Ökosystemen in Abhängigkeit von Klima und Stoffeintrag - Eine regionale Fallstudie auf Landschaftsebene
M. Erhard (Dezember 1999)

No. 57 Response of a River Catchment to Climatic Change: Application of Expanded Downscaling to Northern Germany
D.-I. Müller-Wohlfeil, G. Bürger, W. Lahmer (Januar 2000)

No. 58 Der "Index of Sustainable Economic Welfare" und die Neuen Bundesländer in der Übergangsphase
V. Wenzel, N. Herrmann (Februar 2000)

No. 59 Weather Impacts on Natural, Social and Economic Systems (WISE, ENV4-CT97-0448) German report
M. Flechsig, K. Gerlinger, N. Herrmann, R. J. T. Klein, M. Schneider, H. Sterr, H.-J. Schellnhuber (Mai 2000)

No. 60 The Need for De-Aliasing in a Chebyshev Pseudo-Spectral Method
M. Uhlmann (Juni 2000)

No. 61 National and Regional Climate Change Impact Assessments in the Forestry Sector - Workshop Summary and Abstracts of Oral and Poster Presentations
M. Lindner (ed.) (Juli 2000)

No. 62 Bewertung ausgewählter Waldfunktionen unter Klimaänderung in Brandenburg
A. Wenzel (August 2000)

No. 63 Eine Methode zur Validierung von Klimamodellen für die Klimawirkungsforschung hinsichtlich der Wiedergabe extremer Ereignisse
U. Böhm (September 2000)

No. 64 Die Wirkung von erhöhten atmosphärischen CO_2-Konzentrationen auf die Transpiration eines Weizenbestandes unter Berücksichtigung von Wasser- und Stickstofflimitierung
S. Grossman-Clarke (September 2000)

No. 65 European Conference on Advances in Flood Research, Proceedings, (Vol. 1 - Vol. 2)
A. Bronstert, Ch. Bismuth, L. Menzel (eds.) (November 2000)

No. 66 The Rising Tide of Green Unilateralism in World Trade Law - Options for Reconciling the Emerging North-South Conflict
F. Biermann (Dezember 2000)

No. 67 Coupling Distributed Fortran Applications Using C++ Wrappers and the CORBA Sequence Type
Th. Slawig (Dezember 2000)

No. 68 A Parallel Algorithm for the Discrete Orthogonal Wavelet Transform
M. Uhlmann (Dezember 2000)

No. 69 SWIM (Soil and Water Integrated Model), User Manual
V. Krysanova, F. Wechsung, J. Arnold, R. Srinivasan, J. Williams (Dezember 2000)

No. 70 Stakeholder Successes in Global Environmental Management, Report of Workshop, Potsdam, 8 December 2000
M. Welp (ed.) (April 2001)

No. 71 GIS-gestützte Analyse globaler Muster anthropogener Waldschädigung - Eine sektorale Anwendung des Syndromkonzepts
M. Cassel-Gintz (Juni 2001)

No. 72 Wavelets Based on Legendre Polynomials
J. Fröhlich, M. Uhlmann (Juli 2001)

No. 73 Der Einfluß der Landnutzung auf Verdunstung und Grundwasserneubildung - Modellierungen und Folgerungen für das Einzugsgebiet des Glan
D. Reichert (Juli 2001)

No. 74 Weltumweltpolitik - Global Change als Herausforderung für die deutsche Politikwissenschaft
F. Biermann, K. Dingwerth (Dezember 2001)

No. 75 Angewandte Statistik - PIK-Weiterbildungsseminar 2000/2001
F.-W. Gerstengarbe (Hrsg.) (März 2002)

No. 76 Zur Klimatologie der Station Jena
B. Orlowsky (September 2002)

No. 77 Large-Scale Hydrological Modelling in the Semi-Arid North-East of Brazil
A. Güntner (September 2002)

No. 78 Phenology in Germany in the 20th Century: Methods, Analyses and Models
J. Schaber (November 2002)

No. 79 Modelling of Global Vegetation Diversity Pattern
I. Venevskaia, S. Venevsky (Dezember 2002)

No. 80 Proceedings of the 2001 Berlin Conference on the Human Dimensions of Global Environmental Change “Global Environmental Change and the Nation State”
F. Biermann, R. Brohm, K. Dingwerth (eds.) (Dezember 2002)

No. 81 POTSDAM - A Set of Atmosphere Statistical-Dynamical Models: Theoretical Background
V. Petoukhov, A. Ganopolski, M. Claussen (März 2003)

No. 82 Simulation der Siedlungsflächenentwicklung als Teil des Globalen Wandels und ihr Einfluß auf den Wasserhaushalt im Großraum Berlin
B. Ströbl, V. Wenzel, B. Pfützner (April 2003)

No. 83 Studie zur klimatischen Entwicklung im Land Brandenburg bis 2055 und deren Auswirkungen auf den Wasserhaushalt, die Forst- und Landwirtschaft sowie die Ableitung erster Perspektiven
F.-W. Gerstengarbe, F. Badeck, F. Hattermann, V. Krysanova, W. Lahmer, P. Lasch, M. Stock, F. Suckow, F. Wechsung, P. C. Werner (Juni 2003)

No. 84 Well Balanced Finite Volume Methods for Nearly Hydrostatic Flows
N. Botta, R. Klein, S. Langenberg, S. Lützenkirchen (August 2003)